DTIC® DEFENSE TECHNICAL INFORMATION CENTER

Information for the Defense Community

DTIC® has determined on 5/18/09 that this Technical Document has the Distribution Statement checked below. The current distribution for this document can be found in the DTIC® Technical Report Database.

☒ **DISTRIBUTION STATEMENT A.** Approved for public release; distribution is unlimited.

☐ **© COPYRIGHTED**; U.S. Government or Federal Rights License. All other rights and uses except those permitted by copyright law are reserved by the copyright owner.

☐ **DISTRIBUTION STATEMENT B.** Distribution authorized to U.S. Government agencies only (fill in reason) (date of determination). Other requests for this document shall be referred to (insert controlling DoD office)

☐ **DISTRIBUTION STATEMENT C.** Distribution authorized to U.S. Government Agencies and their contractors (fill in reason) (date of determination). Other requests for this document shall be referred to (insert controlling DoD office)

☐ **DISTRIBUTION STATEMENT D.** Distribution authorized to the Department of Defense and U.S. DoD contractors only (fill in reason) (date of determination). Other requests shall be referred to (insert controlling DoD office).

☐ **DISTRIBUTION STATEMENT E.** Distribution authorized to DoD Components only (fill in reason) (date of determination). Other requests shall be referred to (insert controlling DoD office).

☐ **DISTRIBUTION STATEMENT F.** Further dissemination only as directed by (inserting controlling DoD office) (date of determination) or higher DoD authority.

Distribution Statement F is also used when a document does not contain a distribution statement and no distribution statement can be determined.

☐ **DISTRIBUTION STATEMENT X.** Distribution authorized to U.S. Government Agencies and private individuals or enterprises eligible to obtain export-controlled technical data in accordance with DoDD 5230.25; (date of determination). DoD Controlling Office is (insert controlling DoD office).

Mathematical Fluid Dynamics of Plasma Flow Control Over High Speed Wings

AFOSR CONTRACT NO. FA9550-07-C-0039

Final Report **

Dr. David Marshall, (Principal Investigator)
Drs. Alexander Fedorov and Victor Soloviev, (Co-Investigators)
Teledyne Scientific and Imaging Company
Thousand Oaks, California

February 2009

****NOTE:** Content of this report duplicates the 2008 Annual Report, which was submitted in December 2008.

David Marshall
Materials & Optics
Tel: 805 – 373 – 4170
E-mail: dmarshall@teledyne.com

TELEDYNE
SCIENTIFIC COMPANY
A Teledyne Technologies Company

1049 Camino Dos Rios
Thousand Oaks, CA 91360

In reply refer to G.O. # 71295

February 27, 2009

AFOSR/NE
Dr. Arje Nachman
875 North Randolph Street
Suite 325; Room 3112
Arlington; VA 22203
arje.nachman@afosr.af.mil

Subject: Mathematical Fluid Dynamics of Plasma Control over High Speed Wings
Progress Report
Contract No. FA9550-07-C-0039

In accordance with Contract FA9550-07-C-0039 please find enclosed the Final Report** covering the period of February 1, 2007 through November 30, 2008

TELEDYNE SCIENTIFIC COMPANY, LLC

David Marshall
Principle Scientist
Materials Technology

cc: technicalreports@afosr.af.mil

**NOTE: Content of this report duplicates the 2008 Annual Report, which was submitted in December 2008.

REPORT DOCUMENTATION PAGE	*Form Approved* *OMB No. 0704-0188*

1. REPORT DATE *(DD-MM-YYYY)*
27-02-2009

2. REPORT TYPE
Final Report

3. DATES COVERED *(From - To)*
02-01-7 to 11-30-08

4. TITLE AND SUBTITLE
Mathematical Fluid Dynamics of Plasma Control over High Speed Wings

5a. CONTRACT NUMBER
FA9550-07-C-0039

5b. GRANT NUMBER

5c. PROGRAM ELEMENT NUMBER

6. AUTHOR(S)
David Marshall, Alexander Federov and Victor Soloviev

5d. PROJECT NUMBER

5e. TASK NUMBER

5f. WORK UNIT NUMBER

7. PERFORMING ORGANIZATION NAME(S) AND ADDRESS(ES)
Teledyne Scientific and Imaging Company
1049 Camino Dos Rios
Thousand Oaks, Calif., 91360

8. PERFORMING ORGANIZATION REPORT NUMBER
G.O. 71295- Final Report

9. SPONSORING/MONITORING AGENCY NAME(S) AND ADDRESS(ES)

10. SPONSOR/MONITOR'S ACRONYM(S)

11. SPONSOR/MONITOR'S REPORT NUMBER(S)

12. DISTRIBUTION/AVAILABILITY STATEMENT

13. SUPPLEMENTARY NOTES

14. ABSTRACT
Develop theoretical models and computational tools for SDBD flow control applications.

15. SUBJECT TERMS

16. SECURITY CLASSIFICATION OF:			17. LIMITATION OF ABSTRACT	18. NUMBER OF PAGES	19a. NAME OF RESPONSIBLE PERSON
a. REPORT	b. ABSTRACT	c. THIS PAGE			David Marshall
unclassified				38	19b. TELEPHONE NUMBER *(Include area code)* 805/373-4170

MATHEMATICAL FLUID DYNAMICS OF PLASMA FLOW CONTROL OVER HIGH SPEED WINGS

AFOSR CONTRACT NO. FA9550-07-C-0039

PI: David Marshall
Teledyne Scientific and Imaging Company
Thousand Oaks California

Report of SDBD and flow control modeling prepared by:
Alexander Fedorov and Victor Soloviev
Moscow Institute of Physics and Technology
Moscow, Russia

Objectives

Major objectives of the project are:

- Develop theoretical models and computational tools for SDBD flow control applications
- With these tools, study feasibility of the delta-wing flow management by SDBD active control

The effort is focused on the following tasks:

1. Theoretically and computationally investigate leading-edge separation, vortex breakdown and other phenomena associated with flow symmetry breaking and decreasing lift to drag ratio for a delta wing at high angles of attack
2. Theoretically and computationally investigate SDBD physics and develop a computational model predicting plasma effects on aerodynamic flows
3. Verify theoretical and computational tools of Tasks 1-2 by comparisons with available experimental data as well as wind-tunnel experiments to be performed in ITAM under EOARD sponsorship
4. Study potential for delta-wing flow control by active control of the pre-separating boundary layer using SDBD along the wing leading edges
5. Address scaling issues to extrapolate wind-tunnel tests to full-scale flight conditions

Major accomplishments of 2008 effort are summarized in what follows.

Status and Major Accomplishments

1. Modeling of surface dielectric barrier discharge

1.1 Background

Interest to the surface dielectric barrier discharge (SDBD) grows permanently due to possible advantageous applications to the boundary-layer flow control. Experimental and theoretical efforts have been focused on parametric studies of SDBD-induced jets inside the boundary layer [1-8]. The discharge models in these analyses are either semi-empirical or based on simplified numerical simulation of the discharge evolution. Parameters of SDBD-induced jets are postulated rather then predicted by self-consistent modeling of the discharge physics. These papers do not provide validation of discharge simulations against direct experimental measurements of the discharge parameters. A major gap in the plasma flow control technology is the lack of self-consistent physics-based theoretical models and robust computational tools that could provide adequate prediction of the heat and momentum sources induced by SDBD. The latter are needed for flow control applications.

An attempt to fill this gap has been made in the framework of physics-based model [9, 10] elaborated under this project in 2007. A computational code predicting the SDBD evolution in atmospheric air has been developed for the cases of constant positive and negative applied voltage. The numerical results agreed with available measurements of the discharge length and the surface charge density. In accord with experimental data, it was shown that the discharge evolves as a streamer for positive electrode polarity. Because of computational time restrictions it was possible to simulate only one half of the discharge streamer phase. This corresponds to approximately 1% of the full SDBD cycle including both streamer and relaxation phases.

The relaxation phase starts when the discharge stops propagating along the dielectric surface. During this phase the discharge plasma decays due to recombination and spatial redistribution in the drift and diffusion processes. Since the relaxation phase takes the most part of SDBD cycle time (few microseconds compared to 30-50 ns of the streamer phase), it produces the dominant aerodynamic effect. Nevertheless, to predict the SDBD aerodynamic forcing both the streamer phase and the relaxation phase should be simulated properly. In this connection, the effort has been focused on modifications of the model [9,10] to treat the full SDBD cycle and predict induced momentum and heat sources required for flow control applications.

1.2 Physical model and governing equations

The discharge simulation has been performed in 2-D approximation for the electrode layout and the coordinate system shown in Fig. 1. Hereafter the top semi-infinite electrode has a height $h_e = 0.1$ mm above the dielectric surface.

The model accounts for three types of charged particles: electrons (n_e), negative O^- ions (n_-) and positive O_4^+, O_2^+ ions (n_i). The positive ions are close to equilibrium resulting only in one type of effective positive ion [9,10]. The transport equations for the charged particles are

$$\frac{\partial n_i}{\partial t} + div\mathbf{J}_i = k_i N n_e - k_r n_- n_i - k_{dr} n_e n_i + S_{ph},\ \mathbf{J}_i = n_i K_i \mathbf{E}, \tag{1}$$

$$\frac{\partial n_-}{\partial t} + div\mathbf{J}_- = 0.22 k_{at} N n_e - k_{dt} n_- N - k_r n_- n_i,\ \mathbf{J}_- = -n_- K_- \mathbf{E}, \tag{2}$$

$$\frac{\partial n_e}{\partial t} + div\mathbf{J}_e = k_i N n_e - k_{dr} n_e n_i - 0.22 k_{at} N n_e + k_{dt} n_- N + S_{ph},\ \mathbf{J}_e = -D_e \nabla n_e - n_e K_e \mathbf{E}, \tag{3}$$

where $\mathbf{J}$ = flux of particles, D, K = diffusion coefficient and mobility respectively, subscripts $e,+,-$ denote electrons, positive and negative ions, $\mathbf{E}$ = electric field.

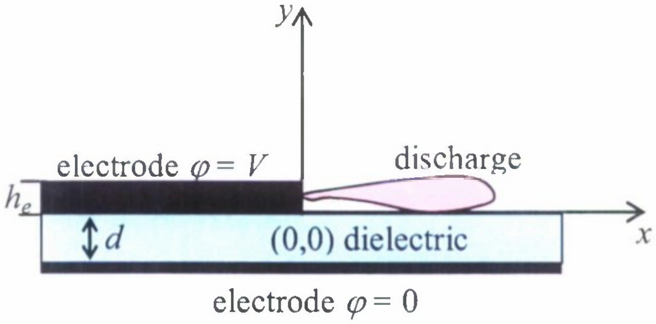

Fig. 1 SDBD electrode layout.

The transport equations are complemented by Poisson equation for the E-field potential φ

$$\Delta\varphi = -4\pi e(n_i - n_- - n_e) \quad \text{for gas region } (y > 0), \tag{4}$$

$$\Delta\varphi = 0 \quad \text{for dielectric layer } (-d < y < 0), \tag{5}$$

$$\mathbf{E} = -\nabla\varphi. \tag{6}$$

Conditions on the gas-dielectric boundary $y = 0, x > 0$ are

$$\left.\frac{\partial\varphi}{\partial x}\right|_{0+} = \left.\frac{\partial\varphi}{\partial x}\right|_{0-},\quad \left.\frac{\partial\varphi}{\partial y}\right|_{0+} = \varepsilon\left.\frac{\partial\varphi}{\partial y}\right|_{0-} - 4\pi\sigma(x,t), \tag{7}$$

where $\sigma = \sigma_e + \sigma_+$ = surface charge density, ε = dielectric permittivity. Boundary conditions for the electric potential are

$$\varphi = 0 \ \text{ for } y = -d, \quad \varphi = V \ \text{ for } 0 < y < h_e,\ x < 0, \tag{8}$$

$$\varphi = V_0\left[\frac{1}{2} - \frac{1}{\pi} arctg\left(\frac{x}{y}\right)\right] \quad \text{for } y \to \infty, x \to \pm\infty, \tag{9}$$

where h_e = upper electrode thickness, d = thickness of the dielectric layer, V = applied voltage. The condition (9) results from asymptotic solution of equation $\Delta\varphi = 0$ in the semi-plane $y > 0$ with the boundary conditions (8) for $d \to 0$.

For typical SDBD parameters corresponding to the discharge thickness ~ 0.1 mm, the electron diffusion flux $D_e \nabla n_e$ is 2-3 orders of magnitude smaller than the drift flux $n_e K_e E$. These fluxes are of the same order of magnitude, when the spatial size of electron density variation is ~ 0.001 mm. Therefore the electron diffusion can be neglected everywhere except a steep discharge front. For ions, the diffusion flux is 4-5 orders of magnitude smaller than the drift flux and can be neglected even at the discharge front. Hence the ion transport equations are hyperbolic and the electron transport equation is parabolic. In accord to the type of equations the boundary conditions for the charged particle concentrations are

$$n_i = n_e = 0, \quad n_- = 0 \quad \text{for } y \to \infty \text{ and } y = 0, \ x \to \pm\infty, \tag{10}$$

$$\begin{matrix} J_{ey} = -K_e n_e E_y - D_e \dfrac{\partial n_e}{\partial y} = 0, & n_i = 0 \\ n_e = 0, \quad n_i = 0 & \end{matrix} \text{, if } \begin{matrix} E_y < 0 \\ E_y > 0 \end{matrix} \quad \text{for } y = 0, \ x > 0 \tag{11}$$

$$n_i = n_- = n_e = 0 \quad \text{for } y = h_e, \ x < 0. \tag{12}$$

The condition (10) stands for the charged-particle densities at infinity. The condition (11) stands for the electron and ion densities on the dielectric surface. For $E_y < 0$, when electrons move away from this surface, it implies that their hydrodynamic flux equals to the flux from the dielectric surface. The latter is assumed to be zero in the condition (11). For $E_y > 0$, when electrons seed the surface, the condition of rapid electron attachment to the surface gives $n_e = 0$. For ions, the condition $n_i = 0$ is valid in both cases because the ion diffusion is negligible and the ion flux from both the dielectric surface and the electrode surface is zero.

The condition (12) indicates that there is no particle flux from the electrode surface. This is always valid for both negative and positive ions. For electrons, the condition (12) is valid only in the case of positive electrode polarity. For negative electrode polarity, it should be replaced by the condition of secondary electron emission from the cathode surface

$$J_{ey} = -\gamma_s J_{iy}, \tag{13}$$

where γ_s = electron secondary emission coefficient.

The balance equations for the surface density of electrons, σ_e, and ions, σ_+, read

$$\frac{\partial \sigma_e}{\partial t} = -J_{ey}, \quad \frac{\partial \sigma_+}{\partial t} = -J_{iy}. \tag{14}$$

The initial conditions are

$$n_i = n_e = n_{in}, \quad n_- = 0, \quad \sigma_e(x,0) = \sigma_i(x,0) = 0 \quad \text{at } t = 0, \tag{15}$$

where n_{in} = background concentration of electrons and positive ions.

The coefficients k_i, k_{dr}, k_r, k_{at}, k_{dt} in Eqs. (1)-(3) designate air ionization, dissociative electron-ion recombination, ion-ion recombination, dissociative electron attachment and detachment rate constants corresponding to the reactions

$$e+\mathrm{N}_2(\mathrm{O}_2)\rightarrow 2e+\mathrm{N}_2^+(\mathrm{O}_2^+),\ k_i=0.78k_{iN_2}+0.22k_{iO_2}=10^{-7.95-\frac{38.22}{\gamma}}\ \mathrm{cm^3/s}, \quad (16)$$

$$e+\mathrm{O}_2^+\rightarrow \mathrm{O}+\mathrm{O},\ k_{dr1}=2\times10^{-7}\left(\frac{300}{T_e(K)}\right)^{0.7}\ \mathrm{cm^3/s}, \quad (17a)$$

$$e+\mathrm{O}_4^+\rightarrow \mathrm{O}_2+\mathrm{O}_2,\ k_{dr2}=1.4\times10^{-6}\left(\frac{300}{T_e(K)}\right)^{0.5}\ \mathrm{cm^3/s}, \quad (17b)$$

$$e+\mathrm{O}_2\rightarrow \mathrm{O}^-+\mathrm{O},\ k_{att}=10^{-10.21-\frac{5.7}{\gamma}}\ \mathrm{cm^3/s}, \quad (18)$$

$$\mathrm{O}^-+\mathrm{N}_2\rightarrow e+\mathrm{N}_2\mathrm{O},\ k_{dt}=9.2\cdot10^{-13}\ \mathrm{cm^3/s}, \quad (19)$$

$$\mathrm{A}^++\mathrm{B}^-+\mathrm{M}\rightarrow \mathrm{A}+\mathrm{B}+\mathrm{M}\quad (\mathrm{M}=\mathrm{O}_2,\mathrm{N}_2),\ k_r=2\times10^{-6}(300/T_i)^{1.5}\ \mathrm{cm^3/s}, \quad (20)$$

where γ = reduced electric field E/N in units of 10^{-16} V·cm^2. The electron temperature T_e and the ion temperature T_i are measured in Kelvin, and the Wannier expression is used to calculate T_i [10]. The appropriate rate constants and expressions for K_e, D_e and T_e were taken from Refs. [11-13]. The ionization rate constants and the electron drift velocity were further corrected to fit to the data [14].

The source term S_{ph} in the right-hand side of Eqs. (1) and (3) refers to gas photoionization by UV radiation from the discharge region. In air, the photo-ionization of O_2 molecules is caused by UV radiation of $N_2(b^1\Pi_u, b'^1\Sigma_u^+, c'_4{}^1\Sigma_u^+)$ excited molecules in the band 98.0-102.5 nm. This source term was taken from the model [15] and its expression was discussed in Refs. [9,10].

In our previous model [9,10] the transport equations were integrated using Particle-in-Cell technique [16] for the drift motion and the grid Gauss elimination (sweep) technique for the electron diffusion. The ion diffusion was neglected. To resolve strong nonlinearity due to the ionization source in the right-hand side of Eqs. (1) and (3), an iteration procedure was used. Relative accuracy of iterations was 10^{-2}. The Poisson equation for the self-consistent electric field potential was solved using the improved Gauss-Seidel (upper relaxation) method with relative accuracy 10^{-5}. Because of steep electric field and electron-ion density gradients relevant to the ionization wave front, the spatial size of computational cell should be less than 1/500 mm. This grid step was used for calculations discussed hereafter.

1.3 Grid technique for transport equations

With the aforementioned numerical approach it was difficult to compute the streamer propagation to distances > 2 mm because of time consuming algorithm. To accelerate computations and increase accuracy of numerical solutions, the Particle-in-Cell technique for the electron drift transport solution has been replaced by the grid method. In this method a computational domain is divided by the grid: $x_i = h_x i$ $(i = 1,...,I)$, $y_j = h_y j$ $(j = 1,...,J)$, where h_x, h_y are steps in x- and y- direction, respectively. The electrical potential $\varphi_{i,j}$ and the electrical charge are determined in the grid nodes. The electric field values are calculated in the mid points as $E_{x,i+1/2,j} = (\varphi_{i+1,j} - \varphi_{i,j}) / h_x$, $E_{y,i,j+1/2} = (\varphi_{i,j+1} - \varphi_{i,j}) / h_y$.

The transport equation

$$\frac{\partial n}{\partial t} - div(nKE) + \ldots, \tag{21}$$

is approximated as

$$\frac{(n^{i,j} - n_{i,j})}{\tau} - \frac{(nKE_x)_{i+1/2,j} - (nKE_x)_{i-1/2,j}}{h_x} - \frac{(nKE_y)_{i,j+1/2} - (nKE_y)_{i,j-1/2}}{h_y} + \ldots \tag{22}$$

where the superscript refers to a quantity on the next time step.

Using "upwind" approximation for the electron drift flux components the electron densities in the mid points are calculated as

$$n_{i+1/2,j} = \begin{cases} n_{i+1,j}\text{, for } E_{x,i+1/2,j} > 0 \\ n_{i,j}\text{, for } E_{x,i+1/2,j} < 0 \end{cases}, \tag{23}$$

$$n_{i,j+1/2} = \begin{cases} n_{i,j+1}\text{, for } E_{y,i,j+1/2} > 0 \\ n_{i,j}\text{, for } E_{y,i,j+1/2} < 0 \end{cases}. \tag{24}$$

The numerical algorithm is implicit, and the stability condition gives the following restriction on computational time steps

$$\tau_x = \min(h_x/(kE_x)), \quad \tau_y = \min(h_y/(kE_y)), \quad 1/\tau = 1/\tau_x + 1/\tau_y. \tag{25}$$

With the grid method computations are quicker and more accurate. However, calculations of streamer evolution to a distance greater than few millimeters were interrupted by numerical instability that occurred near the dielectric surface in the "old" part of the streamer body not far from the electrode edge ($x \approx 0.1$-0.2 mm).

The electron density profiles for the streamer body cross-section $x = 0.1$ mm are shown in Fig. 2. The closer the bottom streamer side to the dielectric surface the greater the electron concentration. This unphysical trend has been observed in numerical solutions obtained with the Particle-in-Cell method as well as the grid method. This could be caused by incorrect modeling of ionization at a sharp front of electron-density and electric-field distributions. In the discussed herein model, the ionization source is a function of the local reduced electric field *E/N*. If the streamer bottom side is close to the dielectric surface, then electrons move against the *E*-field force due to strong diffusion associated with a high concentration gradient and enter to the region of strong *E*-field. In this region, the predicted ionization source is very high and the electron-ion density grows dramatically. The real ionization source can not be so large, because the electrons lose their energy moving against the *E*-field force and can not ionize gas molecules so effectively. Accordingly, a correct ionization model should account for variations of the electron energy in the diffusion process.

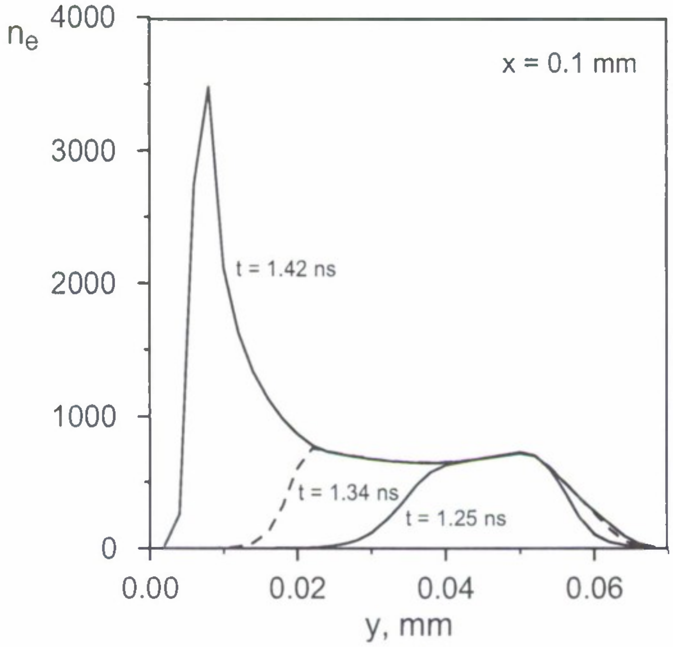

Fig. 2 Instantaneous electron-density n_e/n_0 profiles at the streamer cross-section $x = 0.1$ mm according to numerical solution reported in Refs. [9, 10]; $n_0=0.82\times10^{12}$ cm^{-3}.

1.4 Refinements of physical model

1.4.1 Corrections of ionization source and diffusion flux

If the E-field is strongly inhomogeneous in space, then the ionization rate constant should be obtained from solutions of the inhomogeneous Boltzmann kinetic equation. Nevertheless, a reasonable estimate of this rate constant can be made using the energy conservation equation for electrons. This equation for the electron average energy $\bar{\varepsilon}$ reads [17]

$$n_e \frac{\partial \bar{\varepsilon}}{\partial t} - \left(K_e n_e \mathbf{E} + \nabla\left(D_e n_e\right)\right)\nabla \bar{\varepsilon} - e\left(K_e n_e \mathbf{E} + \nabla\left(D_e n_e\right)\right)\mathbf{E} = -\eta k_{i\_nl} n_e N - n_e W_{el}\,, \tag{26}$$

where η = effective electron energy loss due to all inelastic processes, $n_e W_{el}$ = total electron energy sink associated with quasi-elastic collisions, k_{i_nl} = new non-local ionization rate constant. The first two terms in the left-hand side of (26) refer to an average electron energy variation due to spatial drift and diffusion. The third term describes the electron energy increase because of the work produced by the E-field force. Assuming that this energy is predominantly balanced by inelastic losses, we get an approximate equation

$$e\left(K_e n_e \mathbf{E} + \nabla\left(D_e n_e\right)\right)\mathbf{E} = \eta k_{i\_nl} n_e N\,. \tag{27}$$

For the homogeneous case, this balance is written as

$$e K_e n_e E^2 = \eta k_i n_e N \tag{28}$$

and contains the local ionization rate constant k_i used for our previous modeling. From (27) and (28) we can express the non-local ionization rate constant as

$$k_{i\_nl} = k_i\left(1 + \frac{\mathbf{E}\nabla\left(D_e n_e\right)}{K_e n_e E^2}\right). \tag{29}$$

With this correction, numerical solutions become smooth and stable. The instantaneous electron-concentration and electric-field profiles are shown in Figs. 3 and 4. The streamer bottom side moves toward the dielectric surface much slower than in our previous simulations based on the local approximation of ionization rate constant.

The electric-field and electron-concentration gradients have opposite signs near the dielectric surface. The electron diffusion coefficient D_e increases as the E-field grows. Accordingly, electrons following the diffusion flux penetrate to the region with larger D_e.

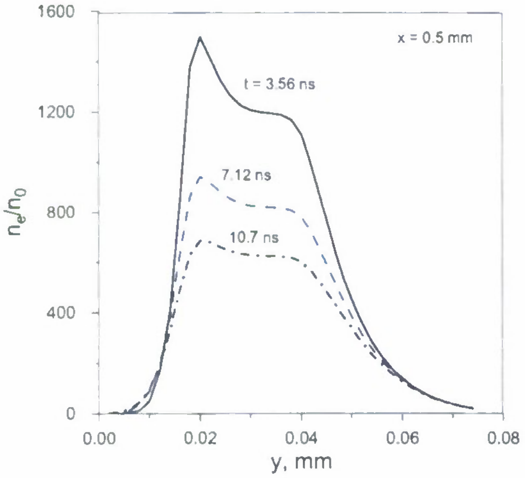

Fig. 3 Instantaneous electron-density profiles at the streamer cross-section x = 0.5 mm, numerical solution with the ionization rate constant (29), n_0=0.82×10^{12} cm^{-3}.

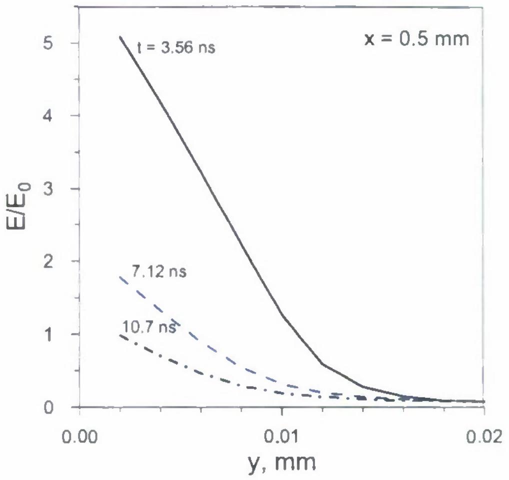

Fig. 4 Instantaneous E-field profiles at the streamer cross-section x = 0.5 mm, numerical solution with the ionization rate constant (29), E_0=40.35 kV/cm.

Sharp E-field gradients and dependence of the diffusion coefficient on E could cause another computational instability associated with incorrect modeling of the diffusion flux in Eq. (3): $J_{dif} = -D_e \nabla n_e$. The correct diffusion flux is expressed as [17]

$$J_{dif} = -\nabla(D_e n_e)\,. \tag{30}$$

The new model comprising the ionization rate constant (29) and the diffusion flux (30) allows us to simulate the discharge evolution from the beginning to the time instant when the discharge stops propagating along the dielectric surface. This was demonstrated for both negative and positive electrode polarities.

1.4.2 Correction of the boundary condition

The boundary condition (11) on the dielectric surface is valid, if the drift flux of electrons or E_y near the dielectric surface does not change sign along the x-axis. This restriction is violated in the case of alternating voltage that leads to a jump of the electron concentration at a point where $E_y = 0$. This interrupts computations, because the needed accuracy can not be achieved in the jump vicinity. A general boundary condition, which is valid for any surface, implies that the hydrodynamic flux equals to the kinetic flux

$$-K_e n_e E_y - \frac{\partial (D_e n_e)}{\partial y} = a(E_y)\frac{n_e V_T}{4} + f_{out} \ , \tag{31}$$

where

$$a(E_y) = \begin{cases} (1-r)\exp\left(\dfrac{K_e E_y \lambda}{T_e}\right) & for\ E_y < 0 \\ (1-r)\left[\exp\left(-\dfrac{K_e E_y \lambda}{T_e}\right) + 4\left(1 - \exp\left(-\dfrac{K_e E_y \lambda}{T_e}\right)\right)\right] & for\ E_y > 0 \end{cases} \tag{32}$$

V_T = electron thermal velocity, λ = electron mean free path, r = surface reflection coefficient for electrons, f_{out} = electron flux from the surface. The latter is zero, $f_{out} = 0$, for the dielectric surface and the anode electrode, and it is $f_{out} = -\gamma_S J_{iy}$ for the cathode electrode. The condition (31) smoothly varies with E_y and, in the limit of high E_y, tends to the condition (11). The expression (32) was derived using phenomenological estimates of the electron flux at a distance from the surface being less than the mean free path. These estimates are based on elementary kinetic considerations. If $E_y = 0$ and $r = 0$, then $a(E_y) = 1$ and the electron flux to the surface equals to the thermal flux $n_e V_T / 4$.

1.5 Numerical results of SDBD modeling

The SDBD evolution has been computed using the new physical model with the aforementioned corrections of the ionization source, the electron diffusion flux and the boundary conditions. The grid technique described in Section 1.3 is used for numerical integration of the drift transport equations. These refinements allow us to simulate both streamer and relaxation phases of the SDBD cycle.

1.5.1 Discharge evolution for negative electrode polarity

The old model [9,10] predicted the following scenario of discharge evolution. First, a small cathode region is formed near the electrode edge. This region is characterized by high ($\sim 10^{15}$ cm^{-3}) electron-ion density with severe charge separation caused by high electric field. Here strong ionization takes place. The born ions drift to the electrode edge whereas electrons drift to dielectric surface. The electrons seed the dielectric surface and create a negative surface charge, which shields the *y*-component of external electric field and slows down the electron motion to the dielectric surface. In the nose part of discharge (near the right-side boundary of the negatively charged part of dielectric surface) the surface charge leads to increasing of the electric field. Ultimately the *E*-field becomes greater than the air ionization threshold and initiates an ionizing wave (streamer). This wave slides over the dielectric surface and creates a thin (~0.01 mm thickness) electron-ion layer on the dielectric surface (Fig. 5a). Accordingly, the old model predicts that, for negative electrode polarity, the discharge evolves as a near-wall streamer. This contradicts to the experimental data [18] showing that the discharge is diffusive.

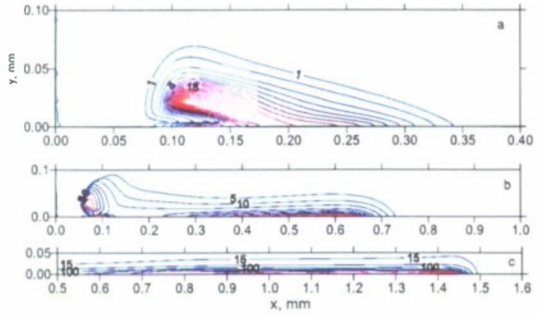

Fig. 5a The old model results for electron density n_e/n_0 contours at different time instants: (a) – t = 6.23 ns, (b) – t =11.6 ns, (c) – t = 14.2 ns; V = - 4.5 kV, ε = 8, d = 1 mm.

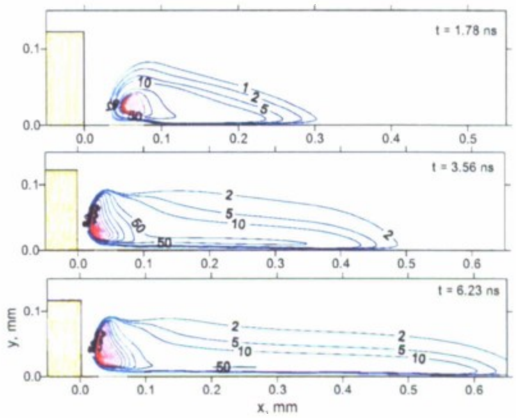

Fig. 5b New model results for electron density contours evolution, yellow region denotes the electrode; conditions are the same as in Fig. 5a.

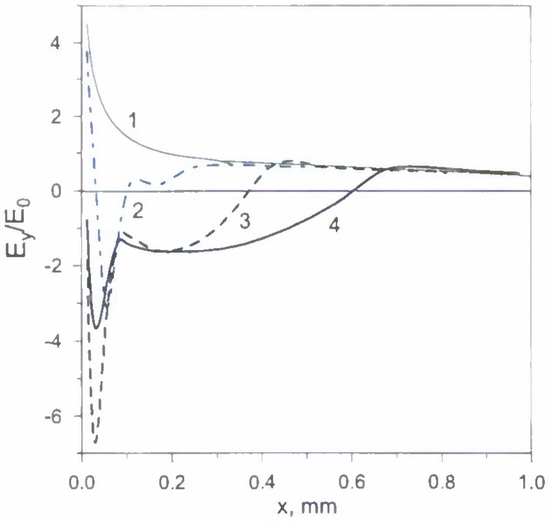

Fig. 6 Instantaneous distributions of $E_y(x)$ on the dielectric surface: (1) – t = 0, (2) – 1.78 ns, (3) – 3.56 ns, (4) – 7.12 ns; V = - 4.5 kV, ε = 8, d = 1 mm, E_0 = 40.35 kV/cm.

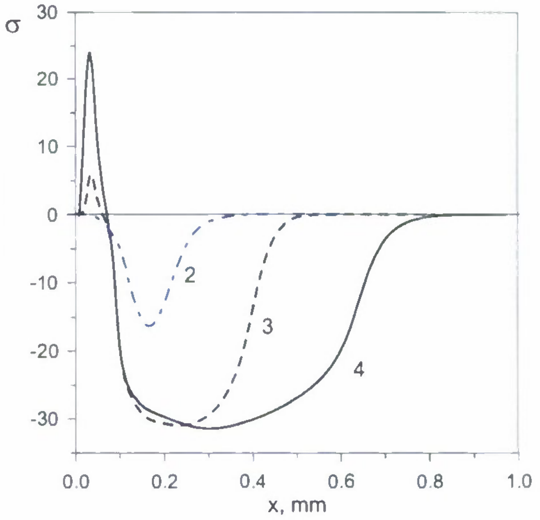

Fig. 7 Instantaneous distributions of the surface charge density $\sigma(x)$ in units of nC/cm^2: (2) – 1.78 ns, (3) – 3.56 ns, (4) – 7.12 ns; V = - 4.5 kV, ε = 8, d = 1 mm.

The new model predicts that there is no ionizing wave moving along the dielectric surface. The initial stage is the same as in the old case – electrons born inside the cathode region start to seed the dielectric surface. However the electric field induced in the discharge nose is not high enough to trigger an ionizing wave (Fig. 5b), and the near-surface layer is formed in a different way: Initially, the E_y component is positive on the dielectric surface for all $x > 0$ (curve 1 in Fig. 6) that corresponds to zero surface charge. In accord with the boundary condition (31), the increase of negative surface-charge density corresponding to J_{ey}<0 continues until E_y changes its sign. Then the drift electron flux becomes positive and high enough to compensate the electron diffusion flux to the surface. Ultimately the total flux tends to zero. Figures 6 and 7 show temporal evolutions of the E_y component on the dielectric surface and the surface charge density at V = -4.5 kV. The E_y component becomes negative over the surface part with high enough charge and ultimately tends to an asymptotic value corresponding to zero flux of electrons to the dielectric surface. The instantaneous distributions of $E_y(x)$ (Fig. 6) correlate with the surface charge density distributions $\sigma(x)$ shown in Fig. 7. The predicted value of σ agrees with the experimental data [18].

In the aforementioned process of near-surface layer formation, the electric field inside this layer (see curves 3, 4 in Fig. 6 and Fig. 8a) is higher than the ionization threshold field E_{th} (E_{th} = 32.28 kV/cm, E_{th} /E_0 = 0.8 for atmospheric air, E_0 = 40.35 kV/cm). This leads to additional ionization, which occurs allover the layer length in contrast to the old model predicting ionization in the streamer head only. Accordingly, the new model gives a *diffusive* discharge for *negative electrode polarity* that agrees with the experimental data [18].

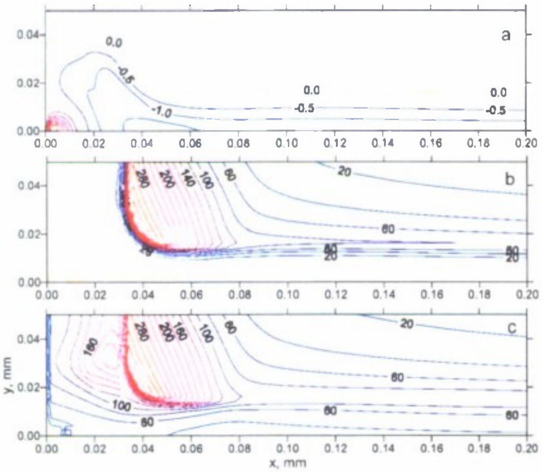

Fig. 8 SDBD structure in the near-electrode region at t =11.6 ns: (a) – E_y/E_0 contours; (b) – electron density n_e/n_0 contours; (c) – positive ion density contours; V = - 5 kV, ε = 8, d = 1 mm; n_0=0.82×10^{12} cm^{-3}, E_0 = 40.35 kV/cm.

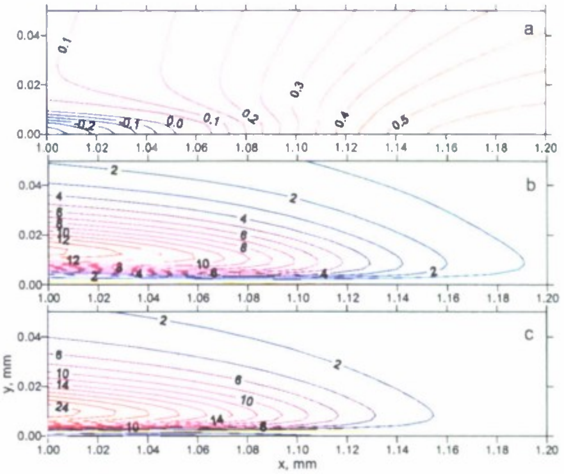

Fig. 9 SDBD structure in the discharge nose region at t =11.6 ns: (a) – E_y/E_0 contours; (b) – electron density contours; (c) – positive ion density contours; conditions are the same as in Fig. 8.

Spatial distributions of SDBD parameters are shown in Figs. 8 and 9 at a time instant that is close to the moment when discharge stops propagating along the dielectric surface. These results were obtained at V = - 5 kV, ε = 8, d = 1 mm, the grid step h = 0.002 mm. A thin plasma layer is formed near the dielectric surface. The electron and ion concentrations inside this layer approximately equal to $5\times10^{13}\,\text{cm}^{-3}$. The layer thickness smoothly decreases from 0.02 mm at $x \approx 0$ to 0.01 mm at the discharge nose. There is no evidence of a streamer head – smooth decreasing of the electron-ion concentration toward the discharge nose is observed (Fig. 9).

The cathode layer is clearly visualized by the electron density contours in Fig. 8b. Formation of a new local maximum in the positive ion density distribution (Fig. 8c) is associated with the beginning of cathode-layer decay. In this stage, the electron-ion recombination inside the cathode layer becomes greater than ionization, and the charged particle concentration starts decreasing. This process combined with the ion drift toward the electrode edge results in the aforementioned local maximum.

Note that even at the beginning of cathode-layer decay the electric field inside this layer is much greater than the air threshold ionization value (E_{th} = 32.28 kV/cm, $E_{th}/E_0 = 0.8$ for atmospheric air). Nevertheless, the ionization source is small because the electron density is low in the cathode layer.

1.5.2 Discharge evolution for positive electrode polarity

For positive electrode polarity, the streamer evolution predicted by the new model is also different from that reported in Refs. [9,10]. As contrasted to the old model, the streamer does not 'touch' the dielectric surface (Fig. 10). Its velocity approximately 2.8 times larger compared to the old case. The streamer parameters do not vary notably after the streamer formation – the electron density contours for the streamer nose, which are shown in Fig. 10 at t = 7.12 ns and t = 14.2 ns, practically coincide.

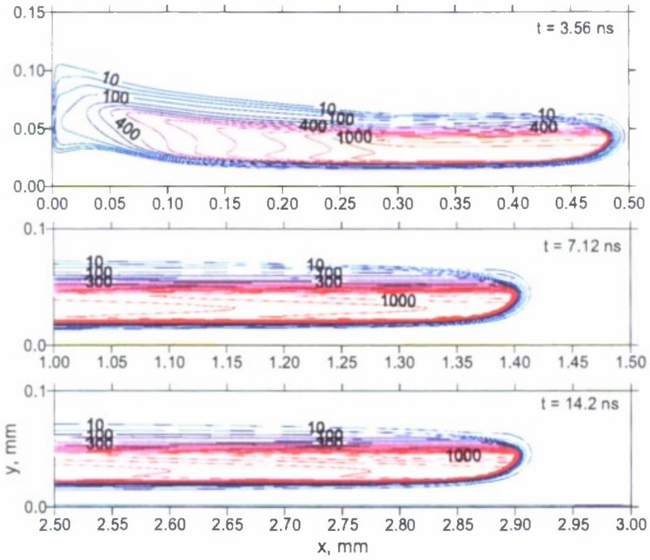

Fig. 10 Streamer evolution predicted by new model; electron density n_e/n_0 contours at $V = +4.2$ kV, $\varepsilon = 8$, $d = 1$ mm.

Although the streamer does not touch the dielectric surface, the surface charge density (associated with the ion drift to the dielectric surface) decreases only twice compared to the old solution [10]. Figure 11 shows that the new distribution $\sigma(x)$ agrees better with the experiment [18].

The experimentally observed streamer length (Fig. 12) for positive electrode polarity increases with the applied voltage. Its minimal value is around 8 mm under the near breakdown condition $V \approx 4$ kV. Unfortunately, Ref. [18] did not provide the dielectric layer thickness d and its permittivity ε for the data in Fig. 12. In our calculations we used $d = 1$ mm and $\varepsilon = 8$, which were reported in Ref. [18] for another data set. In accord with experimental observations, the numerical solution shows that the streamer breakdown in atmospheric air has a threshold nature. If the applied voltage is below a certain level, then the streamer is not formed and the discharge just glows near the electrode edge and rapidly decays. According to our calculations the breakdown threshold voltage is ≈4.2 kV for atmospheric air. At this voltage the calculated streamer length is ≈8 mm, when the discharge stops moving along the dielectric surface and starts decaying. As shown in Fig. 12, this prediction agrees well with the experiment [18].

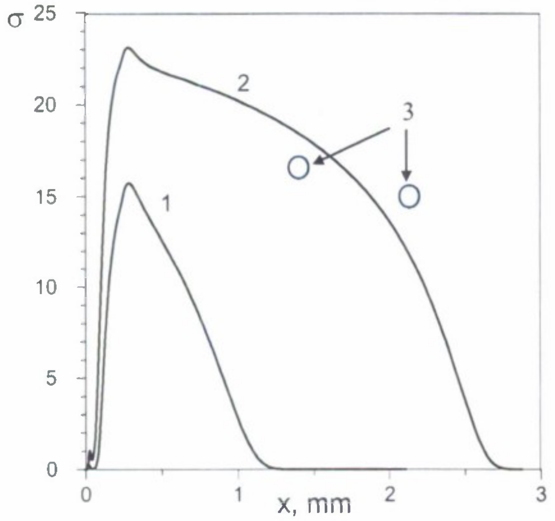

Fig. 11 Surface charge density σ in units of nC/cm^2 for streamer evolution; (1) – t = 7.12 ns, (2) - t = 14.2 ns, (3) – experiment [18]; V = +4.2 kV, ε = 8, d = 1 mm.

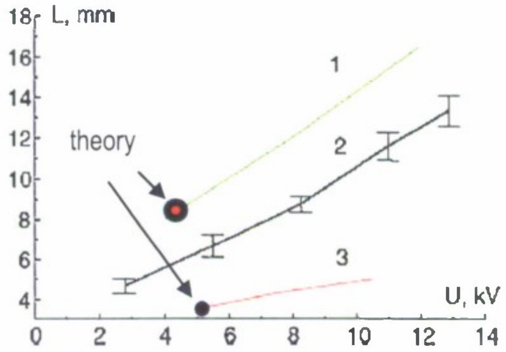

Fig. 12 Experimentally observed SDBD length in atmospheric air at different applied voltage [18]: (1) – constant voltage of positive polarity, (2) – alternating voltage, (3) – constant voltage of negative polarity. Symbols show predictions of the new model at V = +4.2 kV and V = -5 kV ($V \equiv U$).

For constant applied voltage, the streamer length is so large that it is extremely time consuming to simulate the streamer relaxation phase. To shorten a streamer length we reduced the applied voltage after the streamer has been formed (Fig. 13).

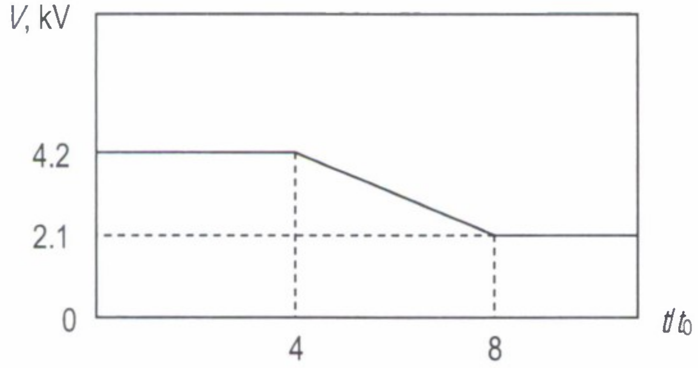

Fig. 13 Applied voltage profile used for shortening of the streamer length.

1.6 Modeling of relaxation phase

The relaxation phase begins when the discharge plasma shields the external electric field to a value less than the air ionization threshold and/or the electron density becomes small inside regions with high electric field. In both cases the ionization source becomes negligible in the discharge region.

It is prudent to use different approaches for simulation of the discharge formation phase and the discharge relaxation phases, since these phases are associated with different physical processes of different time scales. In the discharge formation phase, the air ionization is a key process for both negative and positive electrode polarity. Ionization creates electron-ion pairs inside a high electric field region with initially available electrons. The ionized region polarization in the external electric field generates new spatial distributions of the *E*-field and the charged particle concentrations. This process is governed by Eqs. (1)-(5) without any simplification. The characteristic time of the discharge formation phase is time of the electron drift to the ionization length (ionization time). The typical time step for simulation of the discharge formation is approximately 10^{-13} s.

In the relaxation phase, the ionization source becomes notably less than the divergence of electron drift flux allover the discharge region

$$\nabla(n_e K_e \mathbf{E}) >> k_{ieff} N n_e \,. \tag{33}$$

Since the ionization source is negligible and the electron drift time is small compared to the time of other inelastic processes (electron-ion recombination, electron detachment), the transport equation (3) for electrons splits into two equations: the balance equation (34) for absolute values of the electron density and Eq. (35) governing spatial redistributions of electrons. Fast electron redistribution occurs in the electric field generated by slow ion motions governed by Eq. (36). Accordingly, the system of equations (1)-(3) is reduced to the system

$$\frac{\partial n_e}{\partial t} = k_i N n_e - k_r n_e n_i - 0.22 k_{at} N n_e + k_{dt} n_- N \,, \tag{34}$$

$$\nabla(D_e \nabla n_e + n_e K_e \mathbf{E}) = 0 \,, \tag{35}$$

$$\frac{\partial n_i}{\partial t} + \nabla(n_i K_i \mathbf{E}) = k_i N n_e - k_r n_e n_i - k_{ri} n_- n_i \,, \tag{36}$$

$$\frac{\partial n_-}{\partial t} = 0.22 k_{at} N n_e - k_{dt} n_- N - k_{ri} n_- n_i \,. \tag{37}$$

Poisson equation for the electric potential and the boundary conditions remain the same.

The system (34)-(37) is solved numerically as follows. First, distributions of the ion concentration and corresponding electric field are calculated with a time step relevant to the ion drift motion and managed by the ion mobility K_i. For these distributions, Eq. (35) is integrated using the relaxation technique with a much smaller time step.

Because the electron mobility K_e is much larger than the ion mobility K_i, the main time step for numerical simulation of the relaxation phase is $K_e / K_i \sim 500$ times greater than that for the discharge formation phase. It was found that the time step 10^{-10} s is appropriate for simulations of the discharge relaxation phase having the time scale 10^{-6} s.

1.6.1 SDBD relaxation for negative electrode polarity

For V = -5 kV the SDBD relaxation process, which starts with the charged particle and the electric field distributions relevant to the end of discharge formation (Figs. 8 and 9), is illustrated by Figs. 14-16. The beginning of relaxation (t = 35.6 ns) is shown in Fig. 14. Compared to the distributions in Figs. 8, 9 the electron density decreases approximately 3 times and the electron cloud is repulsed from the dielectric surface.

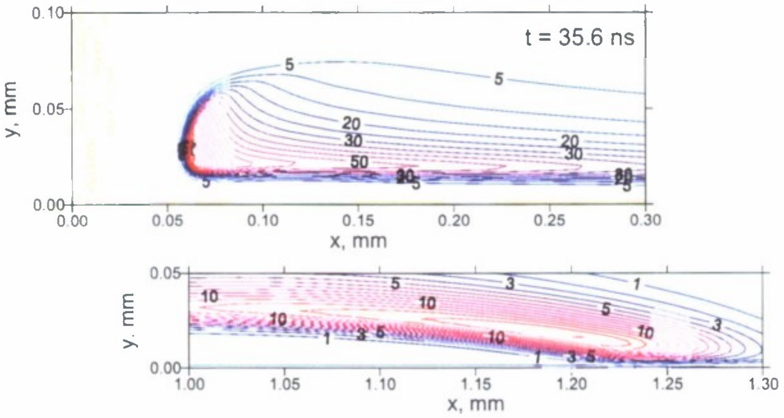

Fig. 14 Electron density n_e/n_0 contours at t = 35.6 ns relevant to the beginning of relaxation phase, V = - 5 kV, ε = 8, d = 1 mm.

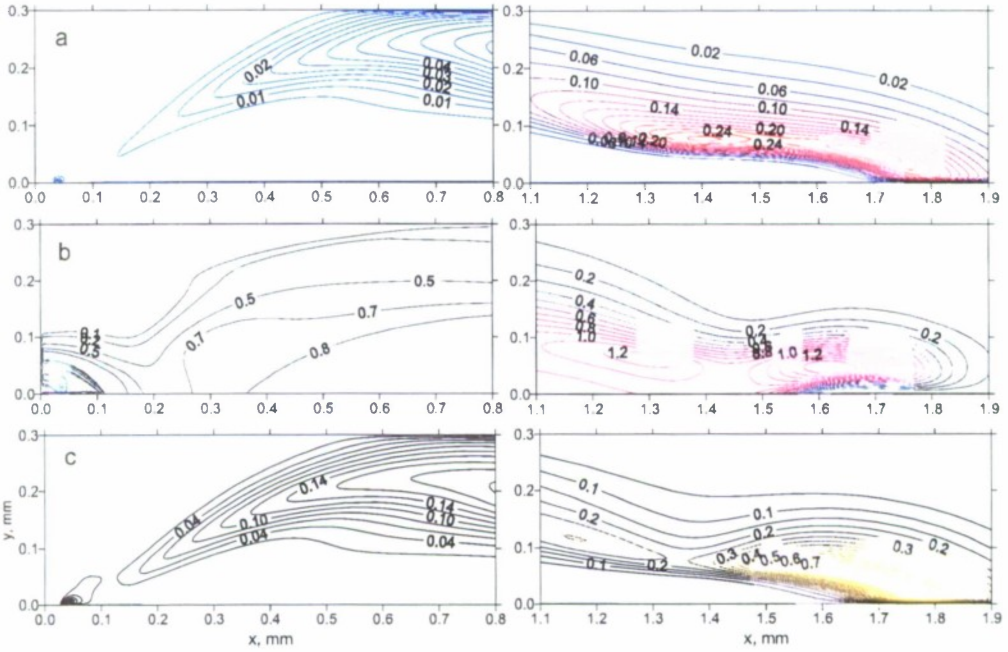

Fig. 15 Density contours for: (a) - electrons n_e/n_0, (b) - positive ions n_i/n_0, and (c) - negative ions n_n/n_0 at t = 0.623 mcs; V = - 5 kV, ε = 8, d = 1 mm.

The electron and ion density distributions at t = 0.623 mcs are shown in Fig. 15 for the near-electrode region and the discharge front. All charged-particle concentrations significantly decrease due to recombination, and the electron density becomes less than densities of positive and negative ions. As contrasted to the discharge formation phase, when plasma was located inside a thin ($\approx$0.02 mm) layer over the dielectric surface, the charged particle cloud moves away from the dielectric surface to a distance ≈ 0.1-0.2 mm. As a result, the volumetric force acting on air due to motions of charged particles, occupies much thicker layer than in the discharge formation phase. The volumetric force is defined as

$$\mathbf{f} = e(n_i - n_- - n_e)\mathbf{E}, \tag{38}$$

and the power input per unit volume is estimated as

$$W = \mathbf{j}\cdot\mathbf{E}. \tag{39}$$

The x- and y-components of time-averaged force (in units of 10^6 din/cm^3) are shown in Fig. 16. Here the red color corresponds to the positive force direction and the blue color – to negative.

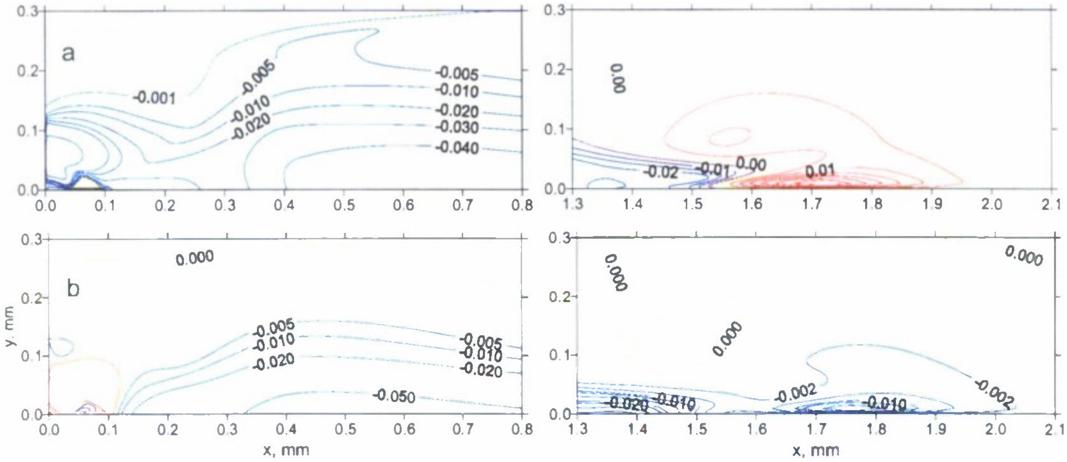

Fig. 16 Contours of time-averaged momentum source components in units of 10^6 din/cm^3 at t = 0.623 mcs, V = - 5 kV, ε = 8, d = 1 mm; (a) – x-component, (b) – y-component.

1.6.2 SDBD relaxation for positive electrode polarity

The applied voltage variation shown in Fig. 13 allows us to slow down the streamer propagation and stop it at a distance $\approx$ 2 mm. Further relaxation of the streamer plasma is illustrated in Fig. 17 at the time instant t = 0.9 mcs. Concentrations of all charged particles decreased by two orders of magnitude compared to the streamer formation phase, they approximately equal to 5×10^{12} cm^{-3}. The electron and positive ion densities are close to each other, while the negative ion density is three orders of magnitude less. Accordingly, the negative charged particle composition of decaying plasma is opposite to the case of negative electrode polarity at which the negative ion density was greater than the electron density.

Figures 18 and 19 show the time averaged, $f = \frac{1}{t_{fin}}\int_0^{t_{fin}} f_{inst}(t)dt$, momentum and heat source contours relevant to the E-field and charged particle distributions shown in Fig. 17. The red color in Fig. 18 corresponds to positive volumetric force, the blue color – to negative. The sign of the x-component of momentum source, F_x, is the same as in the case of negative electrode polarity because E_x-component has the same sign. This is due to the fact that the potential inside the streamer body is approximately equal to the electrode potential by the end of streamer forming. After decreasing of the applied voltage (Fig. 13) the electrode potential becomes less than the potential inside the plasma region (Fig. 17d) and the E_x-component is negative. Coincidence of the force direction with the E-field direction indicates that positive ions primarily contribute to the momentum source.

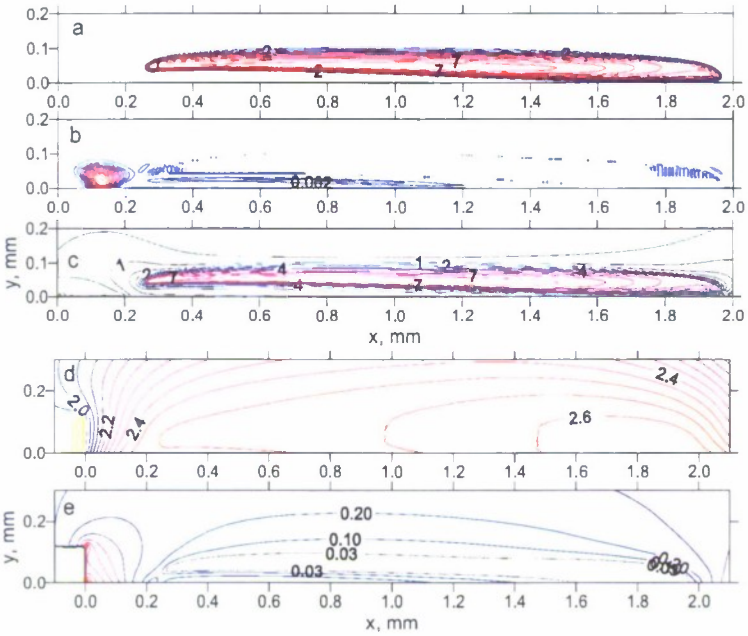

Fig. 17 Contours of: (a) – electron density n_e/n_0, (b) - negative ions density n_-/n_0, (c) - positive ions density n_i/n_0, (d) - potential φ/φ_0 (φ_0= 1.091 kV), and (e) – electric field E/E_0 at t = 0.9 mcs for alternating voltage shown in Fig. 13, ε= 8, d = 1 mm.

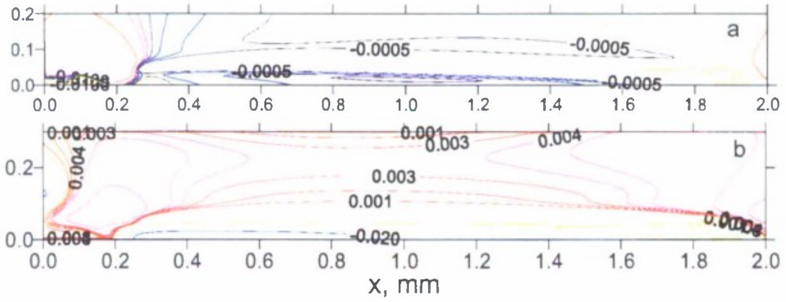

Fig. 18 Contours of time-averaged momentum source components in units of 10^6 din/cm^3 at t = 0.9 mcs for alternating voltage shown in Fig. 13, ε= 8, d = 1 mm; (a) – x-component, (b) - y-component.

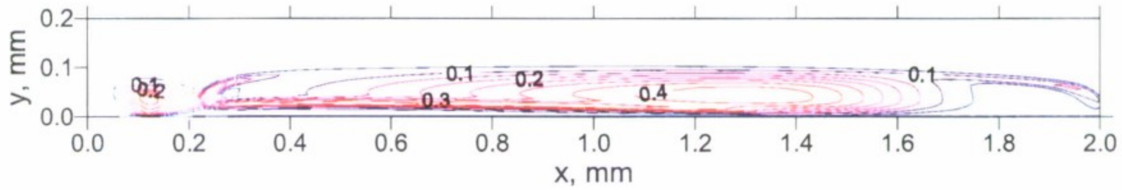

Fig. 19 Contours of time-averaged heat source in units of 10^3 W/cm^3 at t = 0.9 mcs for alternating voltage shown in Fig. 13, ε= 8, d = 1 mm.

As contrasted to the x-component of momentum source, the y-component, F_y, changes its sign when the electrode polarity is changed. An absolute value of both F_x and F_y is greater in the case of negative electrode polarity. However, the momentum-source layer thickness is greater in the case of streamer relaxation after positive applied voltage. Comparing Figs. 18 and 19 we conclude that the heat-source layer approximately 3 times thinner than the momentum-source layer.

Evolutions of E-field and the momentum source distributions during the relaxation phase in the case of decreasing applied voltage are shown in Figs. 20-22. By the end of streamer forming (t = 17.8 ns) and the beginning of relaxation phase (t = 89 ns) the electric field inside the streamer body is close to zero. It starts growing only after a notable plasma decay and appreciable changes of the charge particle balance due to recombination and drift motions (see Fig. 17e for t = 0.9 mcs and Fig. 20 for t = 1.6 mcs).

The E-field increase induced by plasma relaxation is followed by the momentum source formation. At the beginning of relaxation phase the momentum source is not zero only in a small region associated with the past-streamer head (see distributions at t = 0.18 mcs in Figs. 21 and 22). Afterward this region spreads and simultaneously the F_x component arises inside the streamer body – the blue curve appears in Fig. 22 at t = 0.54 mcs. This curve corresponds to F_x = -500 din/cm^3.

Inside the past-streamer body, the F_x component is negative, while in the region located near the ex-streamer head this force is positive. For plasma relaxation at negative polarity voltage, there is only a region with negative force both in x- and y-direction. The aforementioned spatial distributions of the volumetric force associated with plasma relaxation for positive and negative electrode polarity are schematically shown by the blue dashed regions in Fig. 23. The red dashed regions show the heat-source layer. A combination of positive and negative forces shown in Fig. 23 may generate near-surface vortex structures which could effectively force the boundary-layer flow. To check this assumption the numerically predicted momentum and heat sources were approximated by analytical expressions, which were used for calculations of relevant flow fields (see Section 3).

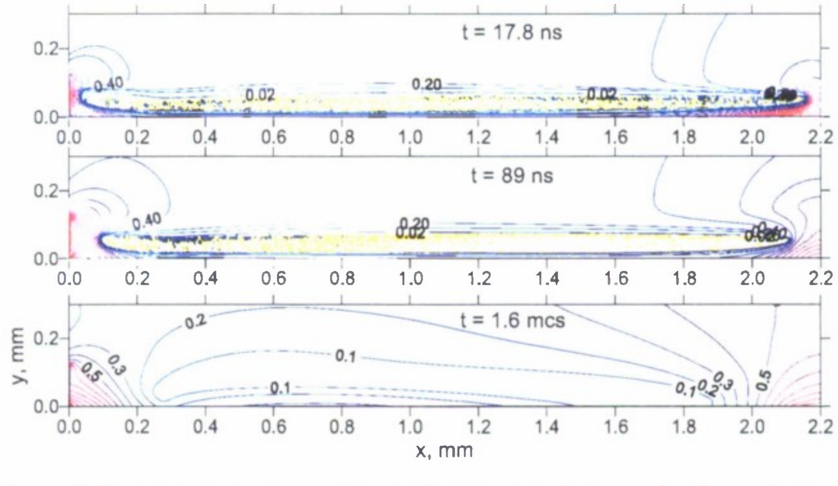

Fig. 20 Dynamics of E/E_0 contours for a streamer relaxation in decreased voltage shown in Fig. 13; ε = 8, d = 1 mm; yellow dots denote E/E_0 = 0.01 .

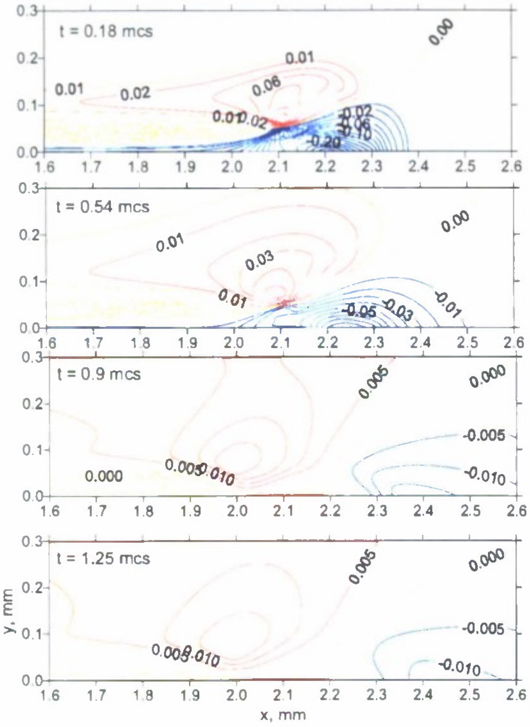

Fig. 21 Contours of the y-component of time-averaged momentum source in units of 10^6 din/cm^3 for streamer plasma relaxation in decreased voltage; $\varepsilon = 8$, $d = 1$ mm.

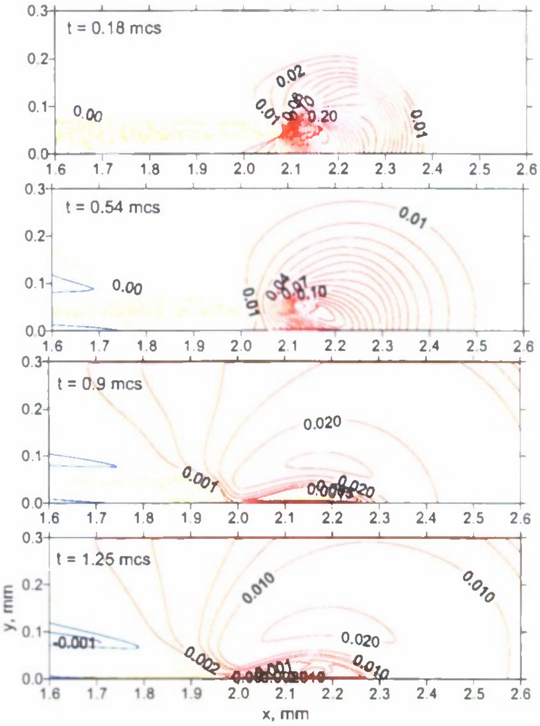

Fig. 22 Contours of the x-component of time-averaged momentum source in units of 10^6 din/cm^3; conditions are the same as in Fig. 21.

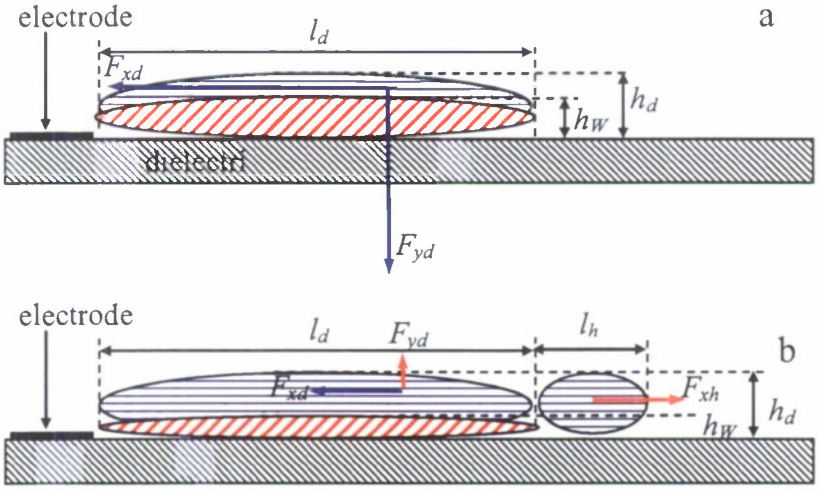

Fig. 23 Schematics of momentum and heat source distributions for relaxation of: (a) - diffusive plasma at negative polarity voltage and (b) - streamer plasma at positive decreased voltage.

2. Modeling of the vortex flow over a supersonic delta wing at angles of attack

We have continued CFD modeling of the SDBD effect on aerodynamics of a supersonic delta wing. The considered wing configuration is shown in Fig. 24: the leading-edge sweep angle $\Lambda = 60°$, the wing thickness is zero, the leading and trailing edges are sharp. Cartesian coordinates (x, y, z) are made nondimensional using the wing centerline chord L^*. Three-dimensional viscous flow past this delta wing has been simulated using 3-D Navier-Stokes solver at the free-stream Mach number $M_\infty = 1.5$, Reynolds number $\mathrm{Re}_\infty = \rho^*_\infty U^*_\infty L^* / \mu^*_\infty = 2\times10^6$ based on the centerline chord $L^* = 1$ m, stagnation temperature $T^*_0 = 300$ K and angles of attack $0° \le \alpha \le 30°$.

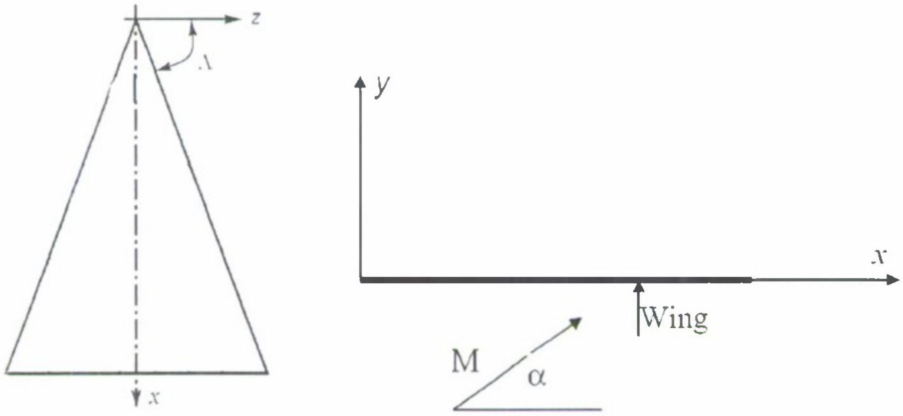

Fig. 24 Delta wing configuration and coordinate system.

Numerical solutions of 3-D Navier-Stokes equations are performed using an implicit finite-volume method. In all cases considered hereafter, the flow is assumed to be laminar. The governing equations are approximated by a conservative scheme. The flux vector is evaluated by an upwind, flux-difference splitting of Roe [19]. MUSCL algorithm is applied with the third order TVD space discretization [20]. An Euler implicit discretization in time of the governing equations is combined with a Newton-type linearization of the fluxes to obtain the system of algebraic equations [21]. This system is solved using a point Gauss-Seidel scheme. The viscosity-temperature dependence is approximated by the Sutherland law

$$\mu^* / \mu^*_\infty = T^{3/2}(1+S)/(T+S)\,,\quad T = T^*/T^*_\infty\,,\quad S = 110.4/T^*_\infty\,, \tag{40}$$

where asterisks denote dimensional quantities, and temperature T^* is measured in K. The fluid is a perfect gas with the specific heat ratio $\gamma = 1.4$ and Prandtl number $\mathrm{Pr} = 0.72$.

The problem is solved for one half of the wing with imposing of the symmetry conditions on the plane $z = 0$. On the outflow boundary, the unknown variables are extrapolated using the linear approximation. On the inflow boundaries, the conditions correspond to undisturbed free stream. The no-slip boundary conditions are imposed on the delta wing surface. Temperature on the wing surface equals to the adiabatic wall temperature. The computational grid has approximately 4.5×10^6 nodes. In the boundary layer and the wing leading-edge region, the grid nodes are clustered to increase resolution of fine flow structures associated with boundary-layer and separation flows.

At high angle of attack the flow field contains two strong vortices generated by the rollup of the shear layer emanating from the separation lines located at the wing leading edges. Since the separation lines are fixed the major effect of plasma forcing is associated with the vortex breakdown (vortex burst). Detailed numerical study of the vortex flow has been performed to estimate feasibility of the vortex breakdown control using SDBD actuators. The following configurations have been treated: the wing-apex SDBD, the leading-edge SDBD and the multi-element SDBD (Fig. 25).

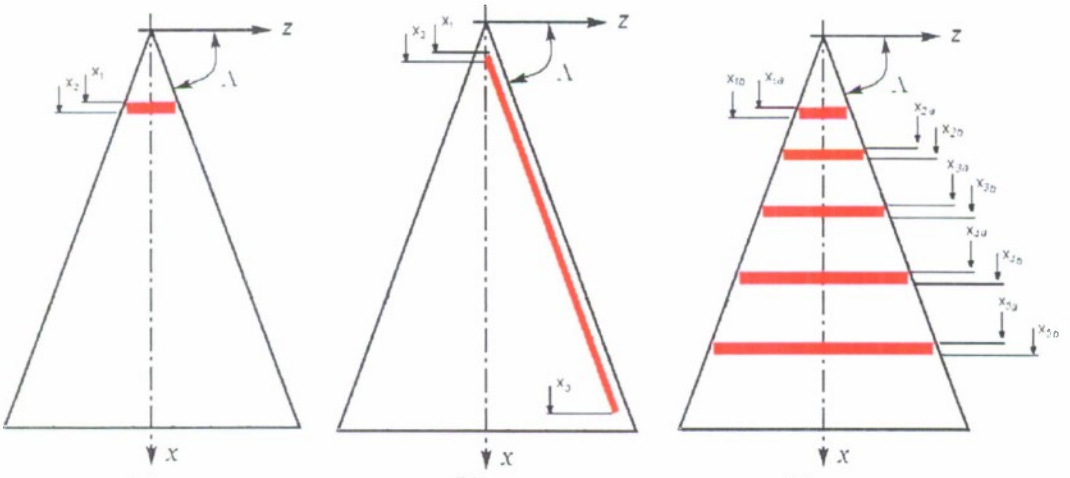

(a) (b) (c)

Fig. 25 Red lines shows SDBD regions for (a) the wing-apex actuator, (b) the leading-edge actuator and (c) the multi-element actuator.

It is assumed that the SDBD actuator generates momentum and heat sources in the region shown by the red strip. From analysis of experimental and computational studies of the SDBD physics Dr. Soloviev suggested the following approximation of these sources. For the wing-apex and multi-element actuators, the volumetric force components are

$$F_x = F_L\,,\ F_L = F_0 f_1(y),\ f_1(y) = \exp\left(-\frac{(y-y_0)^2}{y_0^2}\right), \tag{41}$$

$$F_y = -0.3F_0 f_2(y),\ f_2(y) = \begin{cases} -y(y-2y_0)/y_0^2\,,\ 0 \le y \le 2y_0 \\ 0,\ y > 2y_0 \end{cases}, \tag{42}$$

For the leading-edge actuator, the volumetric force F_L is perpendicular to the leading edge. In this case the streamwise and spanwise components are determined as $F_x = -F_L \cos\Lambda$, $F_z = F_L \sin\Lambda$. The heat source term in the energy equation is approximated as $Q = Q_0 f_1(y)$ within each SDBD strip shown in Fig. 25. For all cases, $F_0 = 10^4\ N/m^3$, $y_0 = 3\times10^{-5}\ m$, $Q_0 = 2\times10^9\ W/m^3$, the width of SDBD strips is 1.5 cm.

2.1 Solutions for the wing-apex actuator

Consider the wing-apex actuator (Fig. 25a) with the leading and trailing edges of SDBD forcing $x_1 = 3$ cm and $x_2 = 4.5$ cm. By changing sign of F_L we simulate SDBD acting downstream ($F_L > 0$) and upstream ($F_L < 0$). In the cases of $\alpha = 0^\circ$ and $\alpha = 5^\circ$, there is no appreciable effect of SDBD on the flow field because there is no global separation from the wing leading edges. For $\alpha = 10^\circ$ (Fig. 26), the SDBD actuator produces a noticeable influence on the wall temperature field and the streamline pattern. First evidence of the vortex breakdown is observed near the wing trailing edge in the case of no SDBD forcing (a).

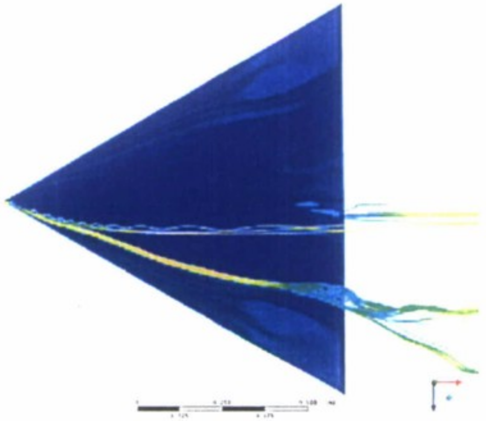

(a) SBD is off

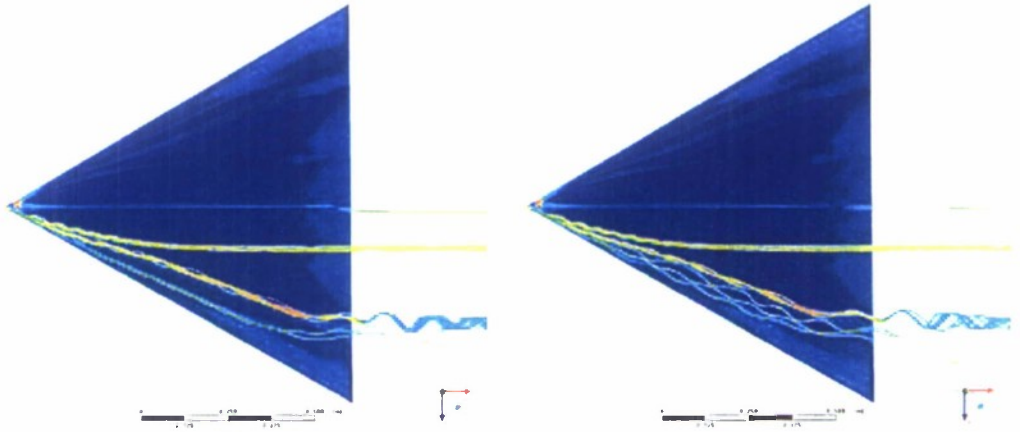

(b) SBD acts downstream (c) SBD acts upstream

Fig. 26 Streamlines and surface temperatures on the leeward side at $\alpha = 10^\circ$.

For $\alpha = 20^\circ$ (SDBD is off) a well-developed vortex is observed in the mid-chord station (Fig. 27a). The burst locus moves downstream with the SDBD acting in the downstream direction (Fig. 27b), while it moves upstream with the SDBD acting in the upstream direction (Fig. 27c). This example demonstrates that the vortex breakdown locus can be controlled by the SDBD forcing near the delta-wing apex. This is consistent with the low-speed modeling of Visbal and Gaitonde [22]. However the integral aerodynamic forces (lift and drag coefficients shown in Figs. 28 and 29) are weakly affected. Presumably the aerodynamic loads at supersonic speeds are not so sensitive to the vortex burst locus. For $\alpha \geq 25°$, the influence of DBD on the vortex breakdown is not so clear, because the breakdown point is very close to the wing apex in all three cases.

For sufficiently high angles of attack, the flow field may evolve with time and the foregoing interpretation should be taken carefully. To clarify this issue we performed direct numerical simulation of unsteady vortex fields for the case of $\alpha = 20°$. As expected the primary vortex breakdown slowly evolves with time. The secondary vortex reveals more unsteady oscillatory behavior. This unsteadiness is observed both with and without SDBD forcing. Nevertheless, appreciable migrations of the burst locus weakly affect the lift coefficient C_L (it varies in the range $0.836 < C_L < 0.840$).

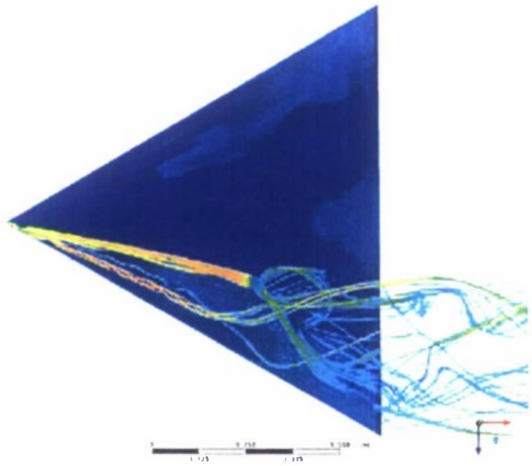

(a) SDBD is off

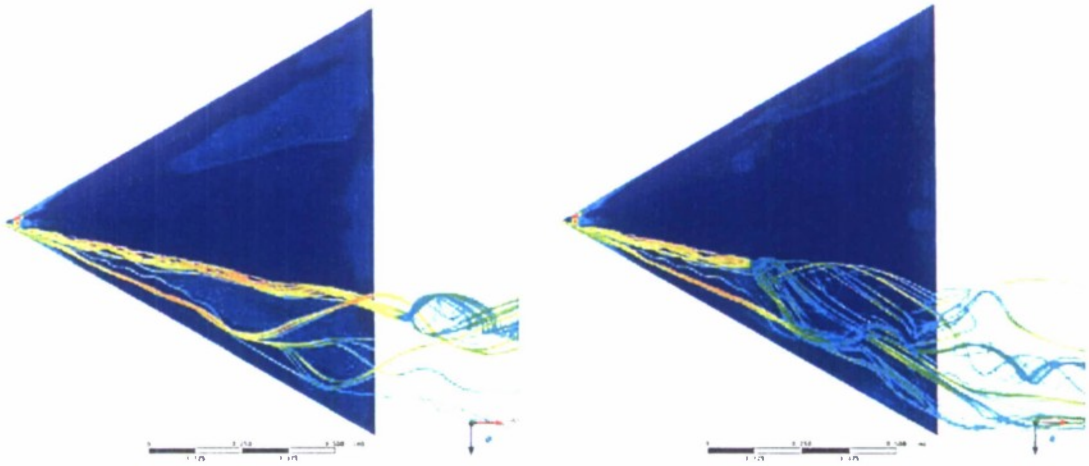

(b) SDBD acts downstream

(c) SDBD acts upstream

Fig. 27 Streamlines and surface temperatures on the leeward side at $\alpha = 20°$.

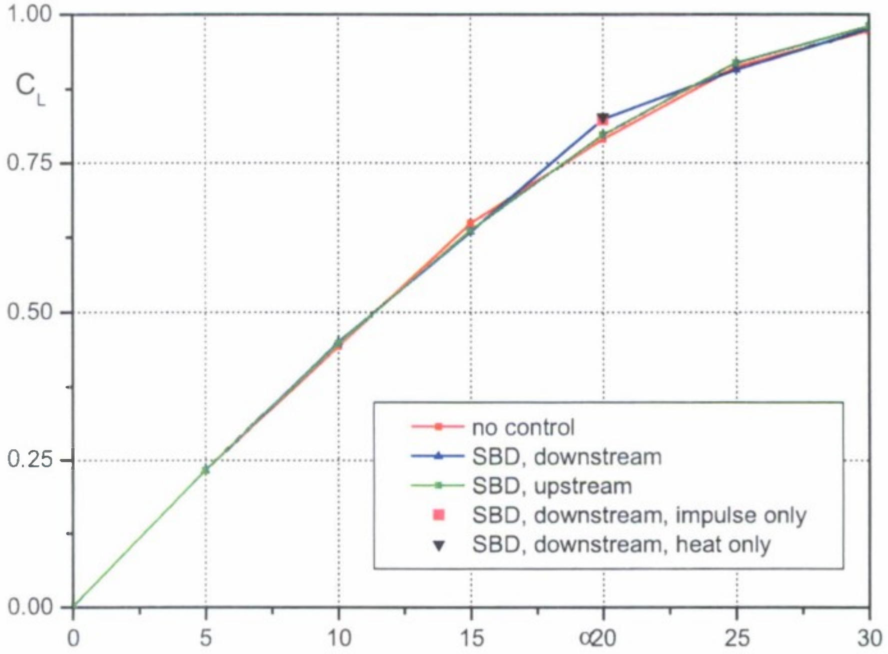

Fig. 28 Lift coefficient versus angle of attack.

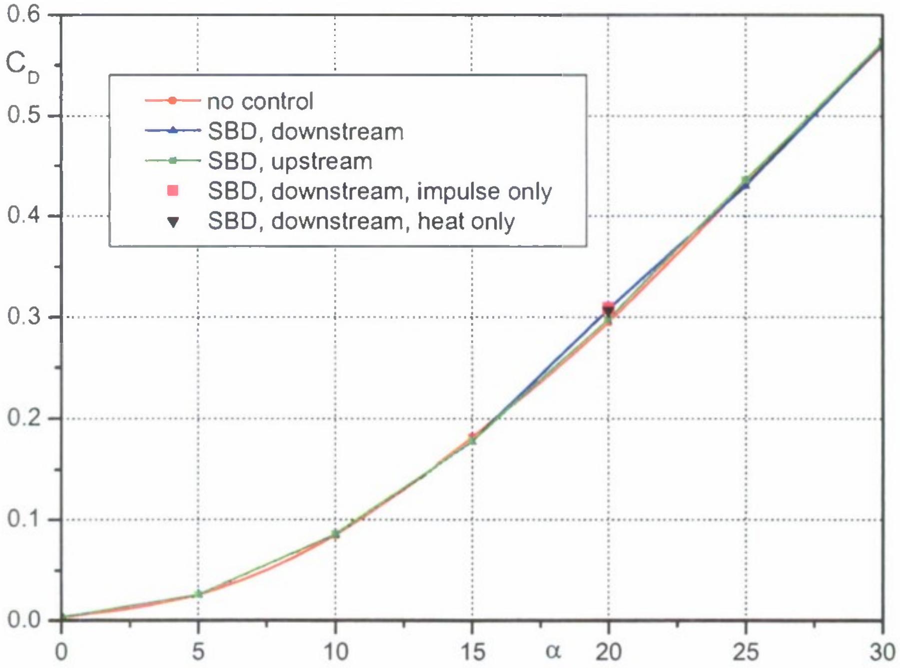

Fig. 29 Drag coefficient versus angle of attack.

2.3 Quasi-steady solutions for the leading-edge actuator

Consider the leading-edge SBD actuator shown in Fig. 25b. The SDBD strip coordinates are specified as $x_1 = 3\,\text{cm}$, $x_2 = 6\,\text{cm}$ and $x_3 = 90$ cm. Figure 30 shows the drag polar, the data of Section 2.2 for the wing-apex actuator are also shown for comparison. In this figure: the red line corresponds to the case of SDBD off; the blue line – to the case when wing-apex SDBD induces the momentum source in the positive x-direction (downstream forcing); the green line – to the case when the wing-apex SDBD induces the momentum source in the negative x-direction (upstream forcing); the magenta square – to the case when the leading-edge SDBD induces the momentum perpendicular to the leading edge at $\alpha = 20^\circ$. Additional computations were carried out to distinguish the SDBD momentum effect from the SDBD heating effect. The black triangle corresponds to the case when the momentum source is included into Navier-Stokes equations while the heat source is not. The cyan triangle corresponds to the opposite situation – the heat source is on while the momentum source is off. In all cases SDBD forcing produces small effect on the wing aerodynamic performance.

Figure 31 illustrates the influence of SDBD on 3-D streamlines and the wall temperature at the angle of attack $\alpha = 20^\circ$. When SDBD is off (Fig. 27a), the vortex burst is observed in the mid-chord station. The momentum source (Fig. 31a) and the heat source (Fig. 31b) lead to an appreciable downstream shift of the vortex burst locus. Nevertheless, this weakly affects the integral aerodynamic forces (Fig. 30).

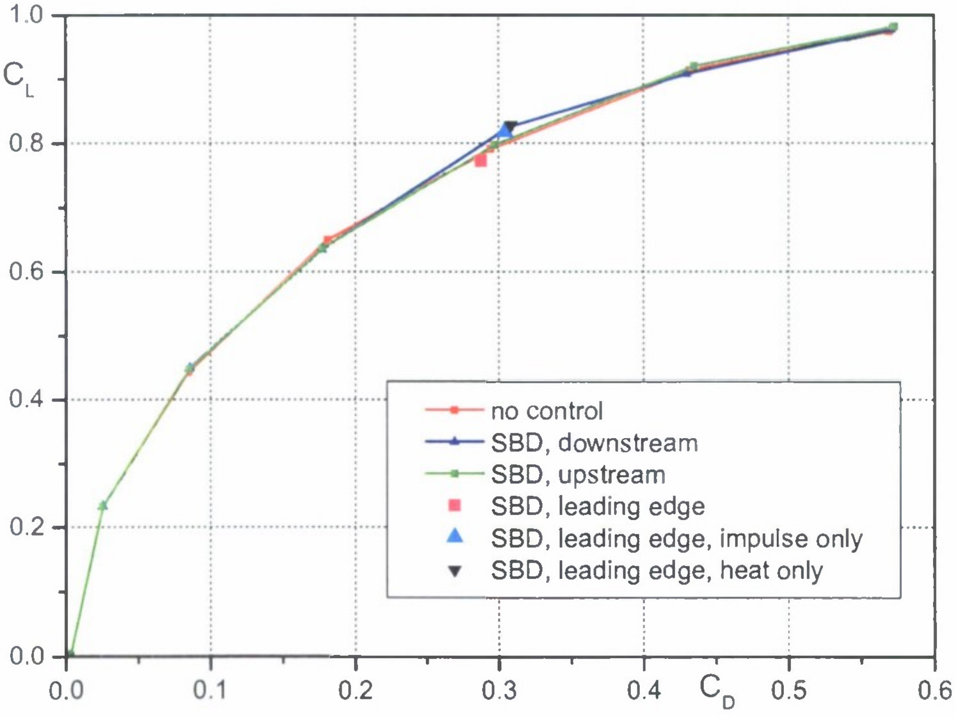

Fig. 30 Drag polar.

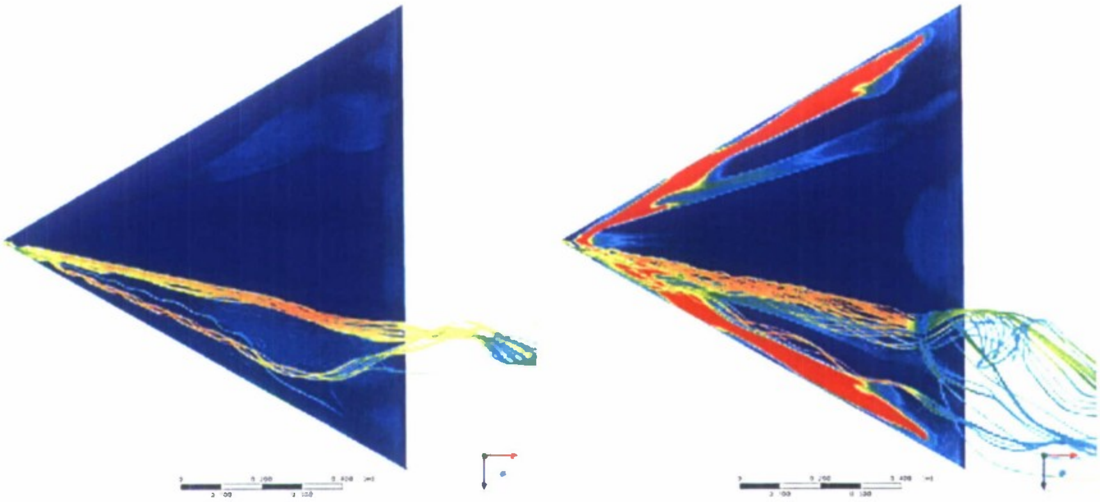

(a) (b)

Fig. 31 The leading-edge SDBD effect on the vortex flow field at $\alpha = 20°$; (a) the momentum source is on while the heat source is off; (b) the heat source is on while the momentum source is off.

2.4 Solutions for the multi-element actuator

Consider the multi-element configuration comprising five SDBD strips (Fig. 25c). This configuration resembles the SDBD actuator used for the low-speed wind tunnel experiments in ITAM [23]. The SDBD strip coordinates, x_{ia} and x_{ib}, are given in Table 1.

Figure 32 shows the five-strip SDBD effect on the flow streamlines and the wall temperature pattern. Similar to the configurations considered in previous sections, the multi-element SDBD actuator causes appreciable downstream shift of the vortex burst. Nevertheless, the integral aerodynamic coefficients vary in the range of 3%.

Table 1

Number of SDBD strip	x_{1a}, m	x_{1b}, m
1	0.03	0.045
2	0.15	0.165
3	0.4	0.415
4	0.6	0.615
5	0.8	0.815

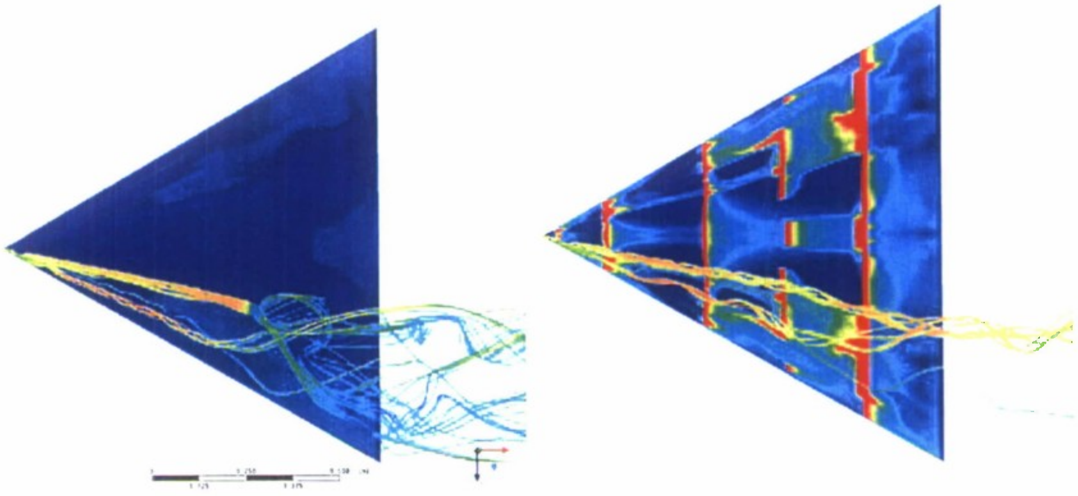

(a) SDBD is off

(b) SDBD is on

Fig. 32 The five-strip SDBD effect on streamlines and surface temperature, $\alpha = 20°$.

3. Modeling of SDBD effect on subsonic flow over a flat plate

The new results of Section 1 indicate that SDBD-induced momentum and heat sources have nontrivial spatial distributions, which are quite different at positive and negative electrode polarities. It is reasonable to assume that such SDBD can produce essentially different aerodynamic effects on the near-wall flow depending on time-distributions of alternating voltage. To verify this assumption we have carried out numerical simulation of the SDBD aerodynamic performance on a flat plate in subsonic free stream.

Consider a laminar flow over a flat plate of length $L = 10$ cm. The free-stream parameters are: velocity $U_\infty = 10\, m/s$, pressure $p_\infty = 10^5\, Pa$, density $\rho_\infty = 1.2\, kg/m^3$ and temperature $T_\infty = 290\,\mathrm{K}$. The fluid is air with the specific heat ratio $\gamma = 1.4$ and Prandtl number $\Pr = 0.72$. The viscosity-temperature dependence is approximated by the Sutherland's law (40). The leading-edge of SDBD region is $x_1 = 2.5$ cm and corresponds to free-stream Reynolds number $\mathrm{Re}_\infty = \rho_\infty U_\infty x_1 / \mu_\infty = 1.73 \times 10^4$ at which the boundary-layer flow is laminar.

2-D compressible Navier-Stokes equations are solved with the following boundary conditions: free-stream conditions on the inflow and upper boundaries of computational domain, 'soft' conditions on the outflow boundary – extrapolation of dependent variables, no-slip conditions on the plate surface, the wall temperature is adiabatic. The computational grid has approximately 2.1×10^5 cells. In the y-direction there are: 300 grid nodes in the boundary-layer region, 40 nodes in the inviscid flow region. In the x-direction there are: 580 grid nodes along the plate surface, 30 grid nodes upstream of the plate leading edge and 20 grid nodes downstream of the plate trailing edge. The grid nodes are clustered the SDBD region $2.5\,\mathrm{cm} \le x \le 3.1\,\mathrm{cm}$.

Without SDBD forcing the numerical solution agrees well with the Blasius solution for laminar boundary-layer flow (Fig. 33).

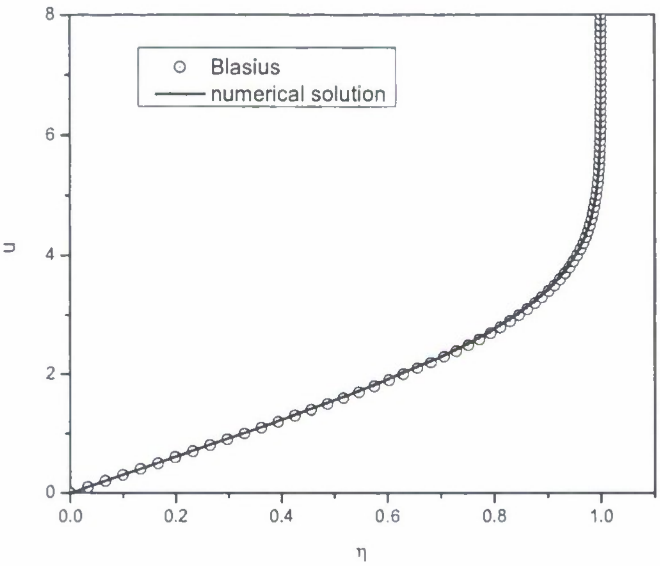

Fig. 33 Boundary-layer profile $u = U(\eta)/U_\infty$ at the station $x = 0.025\,m$, $\eta = y/\sqrt{\nu_\infty x/U_\infty}$.

3.1 Modeling of SDBD momentum and heat sources

As shown in Section 1, the characteristic time-scale of SDBD cycle is of the order of few microseconds. Since the hydrodynamic time-scale is much longer (~ (SDBD length)/U_∞ ~ few milliseconds), it is feasible to modulate the applied voltage by a slow function $\varphi(t)$ of hydrodynamic time-scale as schematically shown in Fig. 34.

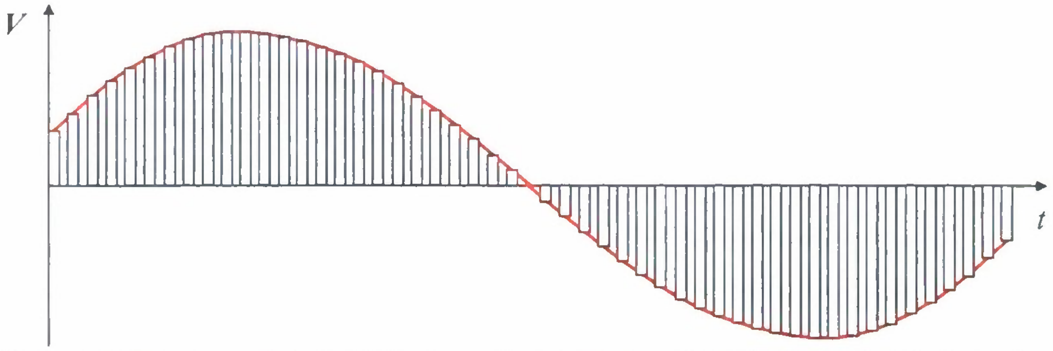

Fig. 34 Applied voltage consists of SDBD cycles with time-scale ~ few microseconds (blue boxes), which are modulated by a relatively slow function $\varphi(t)$ (red line) of hydrodynamic time-scale ~ few msec.

Using results of SDBD modeling discussed in Section 1.6.2, we approximate the volumetric force (F_x, F_y) and heat source Q by the relations

$$F_x(x,y,t) = \varphi(t)\left[F_{xd}(x,y) + F_{xh}(x,y)\right],\, F_y(x,y,t) = \varphi(t)F_{yd}(x,y), \qquad (43)$$

$$Q(x,y,t)=\varphi(t)Q_d(x,t),\tag{44}$$

where

$$F_{xd}=A_{xd}g_d(x)f(y),\,F_{yd}=A_{yd}g_d(x)f(y),\tag{45}$$
$$F_{xh}=A_{xh}g_h(x)f(y),\;Q_d=A_{qd}g_d(x)f_q(y).$$

The functions $g_d(x)$ and $g_h(x)$ are shown in Fig. 35, and the functions $f(y)$ and $f_q(y)$ – in Fig. 36. Their analytical expressions are

$$g_d(x)=\left[1-\left(\frac{x-x_1}{l_d}\right)^2\right]^{0.2},\;x_1\le x\le x_2\tag{46}$$

$$g_h(x)=\left[1-\left(\frac{x-x_2-0.5l_h}{0.5l_h}\right)^2\right]^{0.2},\;x_2\le x\le x_3\tag{47}$$

$$f(y)=A_f y\exp\left[-\frac{\sigma_f\left(y-h_d\right)^2}{2}\right],A_f=7547\,m^{-1},\sigma_f=10^8m^{-2}\tag{48}$$

$$f_q(y)=A_q y\exp\left[-\frac{\sigma_q\left(y-h_W\right)^2}{2}\right],A_q=3\cdot10^4\,m^{-1},\sigma_q=4\cdot10^8m^{-2}\tag{49}$$

where $l_d=5$ mm and $l_h=1$ mm are lengths of the streamer body and the streamer head, respectively; $h_d=0.1$ mm and $h_W=0.005$ mm are vertical sizes shown in Fig. 23b; $x_1=2.5$ cm, $x_2=x_1+l_d$ and $x_3=x_2+l_h$.

The constants A_{xd}, A_{yd}, A_{xh} and A_{qd} in Eq. (45) depend on the type of modulation function $\varphi(t)$. Their values will be specified for different cases considered hereafter.

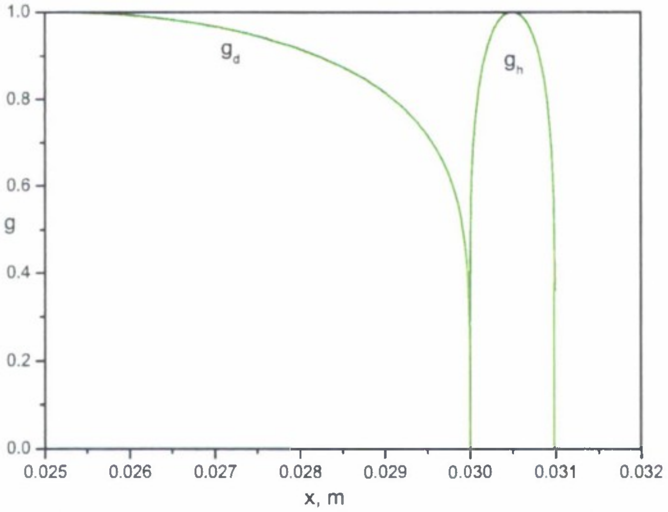

Fig. 35 Longitudinal distribution of momentum and heat sources induced by SDBD at positive voltage polarity.

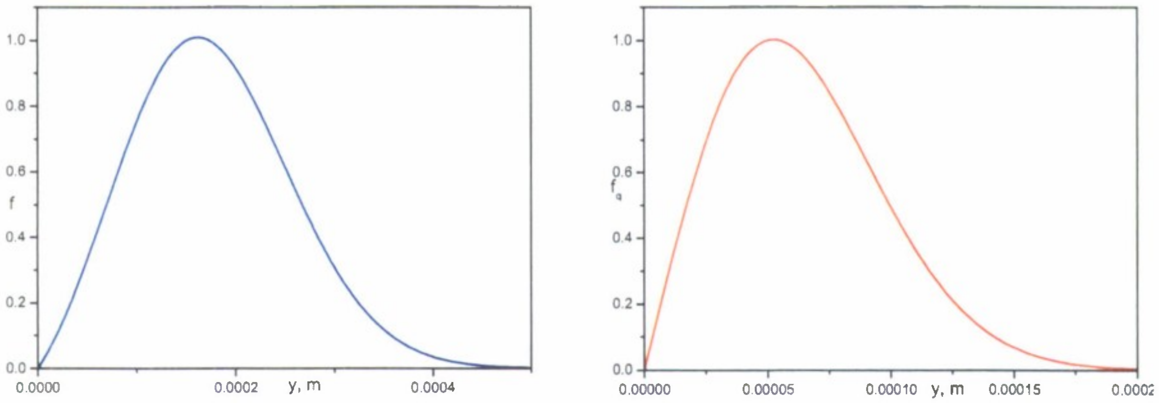

Fig. 36 Vertical distributions of momentum and heat sources induced by SDBD at positive voltage polarity.

3.2 SDBD performance in stationary regime

Consider the case when $\varphi(t)$ is a step-function: $\varphi(t)=0$ for $t \le 0$, $\varphi(t)=1$ for $t>0$. During each SDBD cycle the applied voltage is positive and generates a streamer plasma. The momentum and heat sources are distributes as schematically shown in Fig. 23b. After transient process associated with the actuator switching on, these sources are averaged over the SDBD duty cycle and treated as steady on the hydrodynamic time scale.

The constants in Eq. (45) are evaluated as:

$$A_{xd}=-10^4\ N/m^3\ ,\ A_{yd}=5\cdot 10^4\ N/m^3\ ,\ A_{xh}=2\cdot 10^5\ N/m^3\ ,\ A_{qd}=2\cdot 10^8\ W/m^3\ . \quad (51)$$

The unsteady problem is solved with the time step $5\cdot 10^{-6}\ s$. The numerical solution shows that during the transient process a vortex is generated downstream from the actuator. The vortex penetrates outside the boundary layer and propagates downstream with the local speed of undisturbed flow. Since this speed quickly increases from zero to the free-stream velocity across the boundary layer, the vortical structure is stretched in the longitudinal direction (Fig. 37).

By the time $t \approx 15\times 10^{-4}$ s, the transient process is completed, and a steady flow sets in (Fig. 38). It is seen that SDBD actuator performs as a weakly heated longitudinal jet that accelerates the boundary-layer flow in the downstream direction. The obtained flow velocity increase by 5 m/s correlates with experimentally observed values [5]. Such a tangential jet regime is commonly used for flow control applications.

(a) temperature field (scale from 290K to 350K)

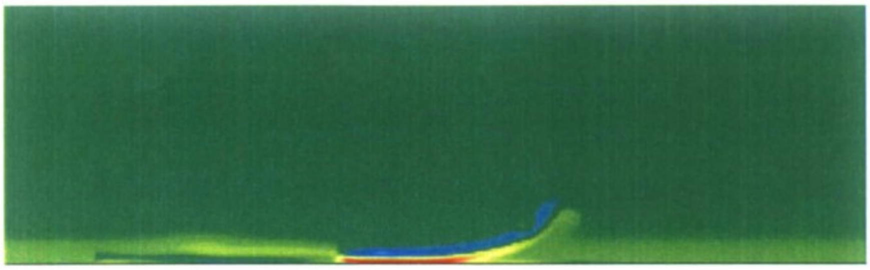

(b) z-component of voticity field (scale from -10^{-5} s^{-1} to $+10^{-5}$ s^{-1})

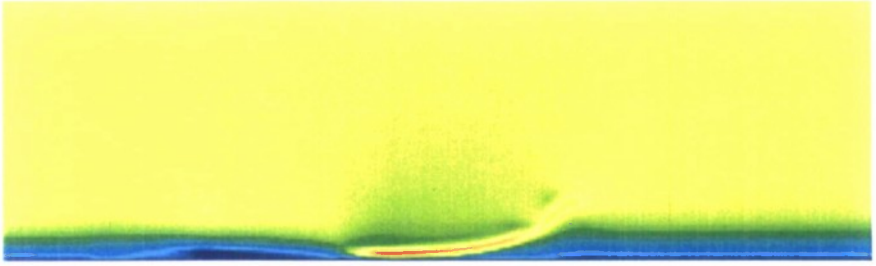

(c) u-velocity field (scale from -1.5 m/s to 15 m/s)

Fig. 37 Flow fields at the time instant $t = 5\times10^{-4}$ s relevant to the transient process.

(a) temperature field (scale from 290K to 350K)

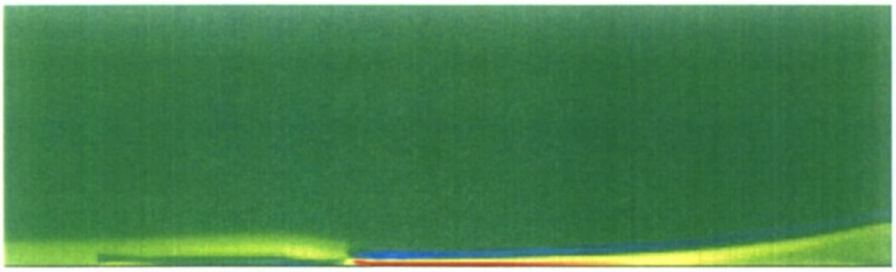

(b) z-component of voticity field (scale from -10^{-5} s^{-1} to $+10^{-5}$ s^{-1})

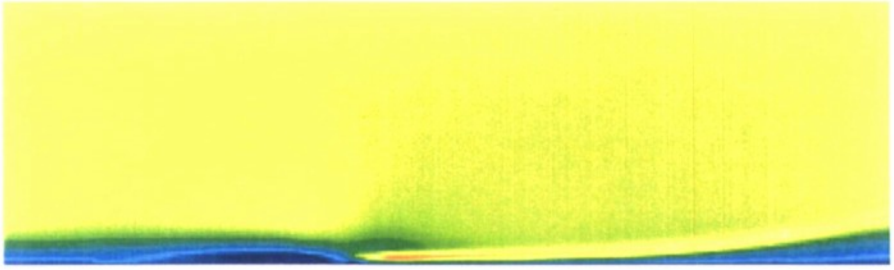

(c) u-velocity field (scale from -1.5 m/s to 15 m/s)

Fig. 38 Steady-state flow fields induced by SDBD, $t = 15\times10^{-4}$ **s.**

3.3 SDBD in periodic regime

Consider the case when $\varphi(t)$ is a periodic step-function: $\varphi(t)=1$ for $0<t<T/2$, $\varphi(t)=-1$ for $T/2<t<T$, where the period is $T=(l_d+l_h)/U_\infty = 6\times10^{-4}$ s. During the first half of period ($\varphi(t)=1$), the actuator generates a streamer-discharge plasma (Fig. 23b) and the constants in Eq. (45) are evaluated as

$$A_{xd} = -3\cdot10^4\ N/m^3\,,\ A_{yd} = 10^4\ N/m^3\,,\ A_{xh} = 2\cdot10^4\ N/m^3\,,\ A_{qd} = 10^7\ W/m^3\,. \tag{52}$$

During the second half of period ($\varphi(t)=-1$), the actuator generates a diffusive-discharge plasma (Fig. 23a) and the constants in Eq. (45) are evaluated as

$$A_{xd} = -4\cdot10^5\ N/m^3\,,\ A_{yd} = -3\cdot10^5\ N/m^3\,,\ A_{xh} = 0\,,\ A_{qd} = 10^8\ W/m^3\,. \tag{53}$$

The unsteady problem is solved with the time step $5\times10^{-6}\ s$. An instantaneous flow field induced by this actuator is shown in Fig. 39. In contrast to the steady regime discussed in Section 3.2, the SDBD actuator works as a vortex generator. During the diffusive discharge phase, the volumetric force is relatively larger and directed upstream. This leads to excitation of strong concentrated vortices near the leading edge of actuator. These vortices penetrate to the outer flow and propagate downstream.

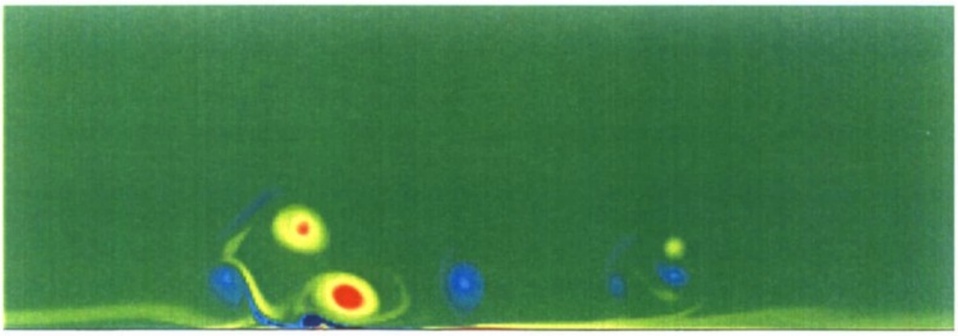

(a) z-component of voticity field (scale from $-10^{-5}\ s^{-1}$ to $+10^{-5}\ s^{-1}$

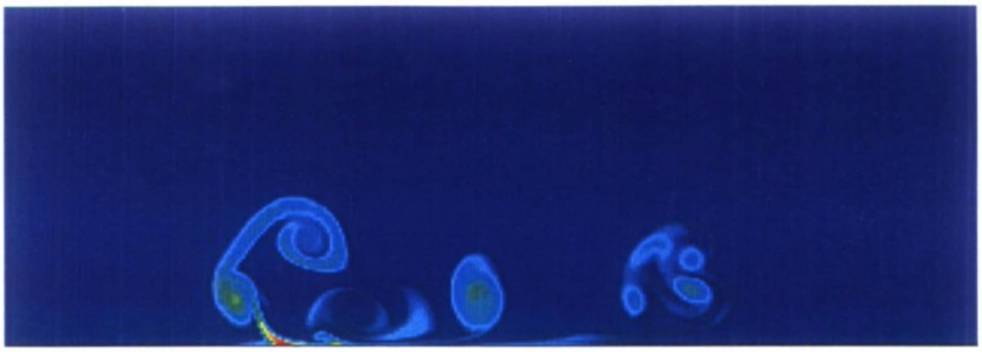

(b) temperature field (scale from 290K to 350K)

Fig. 39 Instantaneous flow field induced SDBD at $t = 20\cdot10^{-4}\ s$.

Summary

1. SDBD modeling

The physical and numerical models developed in 2007 for the surface dielectric barrier discharge (SDBD) in atmospheric air has been improved. The refined model and new computational code allow for simulations of the total SDBD cycle including the discharge formation phase and the discharge relaxation phase.

Numerical studies showed that the discharge formation phase lasts few tens nanoseconds and creates plasma. The discharge evolves as a streamer for positive electrode polarity and as a diffusive discharge for negative electrode polarity. The predicted values of the discharge length and the surface charge density agree well with the available experimental data both for positive and negative electrode polarity. This validates the developed physical model and computational code. Although the discharge formation phase gives negligible contribution to the momentum and heat sources relevant to flow control applications, it provides initial conditions for the relaxation phase.

The relaxation phase begins when plasma is redistributed in such a way that it shields the external electric field and reduces the air ionization rate in the discharge region to very small value. The ion-electron and ion-ion recombination along with the ion drift motion are main processes in the relaxation phase, which lasts few microseconds. This phase effectively contributes to the momentum and heat sources.

The spatial structure and charged particle composition are quite different in the discharge formation and discharge relaxation phases. During the discharge formation plasma occupies a thin near-surface layer of ≈ 0.05 mm thickness for positive electrode polarity (streamer discharge) and ≈ 0.02 mm thickness for negative electrode polarity (diffusive discharge). In the relaxation phase, plasma spreads away the dielectric surface, and the thickness of momentum-source layer increases to ≈ 0.3 mm at both positive and negative electrode polarities. For the case of streamer relaxation at decreasing applied voltage, the thickness of heat-source layer is approximately 3 times less (≈ 0.1 mm), and for negative electrode polarity it is 1.5 times less (≈ 0.2 mm).

The momentum-source distributions have a complex structure in space. For streamer relaxation (at positive applied voltage) the longitudinal component of volumetric force is negative in the ex-streamer body and positive in the ex-streamer head. The length of negative force region depends on the temporal profile and the applied voltage level – it varies from 1 mm to 20 mm. The length of positive force region is approximately 0.3-1.0 mm. For negative electrode polarity there is a region of negative longitudinal component of volumetric force only. The transversal component could be positive or negative inside the ex-streamer body depending on the applied voltage sign and its temporal profile.

2. Flow control modeling

2.1 Supersonic delta wing

Detailed numerical study of the vortex flow past a delta wing with sharp leading edges of 60° sweep angle has been performed to estimate feasibility of the vortex flow control using SDBD actuators. The following configurations have been treated: the wing-apex SDBD, the leading-edge SDBD and the multi-element SDBD. Heat and momentum sources produced by these actuators are modeled by analytical approximations suggested by Dr. Soloviev. Computations have been carried out using 3-D Navier-Stokes solver for the free-stream Mach number $M_\infty = 1.5$, Reynolds number $\mathrm{Re}_\infty = 2\times10^6$ and angles of attack $0^\circ \le \alpha \le 30^\circ$.

Since the boundary-layer separation is fixed (the separation lines are located on the sharp leading edges), the major effect of plasma forcing is associated with the vortex breakdown (vortex burst). It was found that the vortex-burst locus can be controlled by the wing-apex actuator. Namely, the breakdown point moves downstream with the SDBD acting in the downstream direction while it moves upstream with the SDBD acting upstream. However, the integral aerodynamic forces are weakly affected. The actuator causes about 3% variations of the lift C_L and drag C_D coefficients. Presumably the aerodynamic loads are weakly sensitive to the vortex burst locus for the delta wing and free-stream parameters considered herein.

Direct numerical simulation of unsteady flow fields showed that the vortex breakdown locus evolves with time. This unsteady behavior is sensitive to the SDBD forcing. Nevertheless, appreciable migrations of the burst locus produce small (less than 2%) effect on the lift coefficient.

CFD studies showed that the leading-edge and multi-element SDBD actuators cause an appreciable downstream shift of the vortex burst locus. However, the aerodynamic coefficients are weakly affected.

2.2 Subsonic flow over a flat plate

First-cut numerical simulations of the SDBD aerodynamic performance on a flat plate in subsonic free stream have been carried out using the new results of SDBD modeling summarized in Section 1. Numerical solutions of 2-D unsteady Navier-Stokes equations showed that the SDBD actuator can produce essentially different aerodynamic effects on the near-wall flow depending on time-modulations of the applied voltage:

- In a stationary regime with positive applied voltage, the actuator produces a weakly heated longitudinal jet that accelerates the boundary-layer flow in the downstream direction. The obtained flow velocity increase agrees with experimental observations. Such a tangential jet regime is commonly used for flow control applications.
- In a periodic regime comprising the diffusive discharge cycles at negative polarity and the streamer discharge cycles at positive polarity, the SDBD actuator predominantly works as a vortex generator

3. Future effort

The obtained results on SDBD modeling indicate that depending on temporal profiles of the applied voltage it is feasible to produce quite different aerodynamic effects on near-wall flows. These effects need to be understood and sorted out. For each case optimal SDBD parameters should be determined. Scaling issues relevant to extrapolation of wind-tunnel tests to full-scale flight conditions need to be addressed. First this should be done for relatively simple flows, when the SDBD effect is 'clean' and can be well determined.

In this connection we suggest to focus our next-year effort on parametric studies of SDBD performance for the near-wall flow on a flat plate. This basic knowledge will guide SDBD flow control strategies for more complicated aerodynamic configurations.

It is also important to conduct parametric calculations of the momentum and heat sources induced by the SDBD actuator and correlate numerical results by reliable analytical approximations. The latter will be integrated into fluid dynamics tools and used for various flow control applications.

References

[1] Corke, T.C., and Post, M.L., "Overview of Plasma Flow Control: Concepts, Optimization, and Applications," AIAA-2005-563, Reno NV, 10-13 January 2005.

[2] Orlov D.M., Apker T., He C., Othman H., Corke T.C., "Modeling and Experiment of Leading Edge Separation Control Using SDBD Plasma Actuators", AIAA Paper No. 2007-877, Reno NV, 5-11 January 2007.

[3] Boeuf J.P., Lagmich Y., Callegary Th., Pichford L.C., "EHD Force in Dielectric Barrier Discharges Parametric Study and Influence of Negative Ions", AIAA-2007-183, Reno NV, January 2007.

[4] Boeuf J.P., Lagmich Y., Unfer Th., Callegary Th., Pichford L.C., '"Electrodynamic force in dielectric barrier discharge plasma actuators", *J. Phys. D: Appl. Phys.*, V.40, 2007, pp. 652-662.

[5] Moreau E., "Airflow control by non-thermal plasma actuators", *J. Phys. D: Appl. Phys.*, V.40, 2007, pp. 605-636.

[6] Gregory J.W., Enloe C.L., Font G.I., McLaughlin Th.E., "Force Production Mechanisms of a Dielectric-Barrier Discharge Plasma Actuator", AIAA Paper 2007-185, Reno NV, January 2007.

[7] Font G.I., Enloe C.L., McLaughlin Th.E., Orlov D., "Plasma Discharge Characteristics and Experimentally Determined Boundary Conditions for a Plasma Actuator", AIAA Paper 2007-188, Reno NV, January 2007.

[8] Likhanskii A.V., Shneider M.N., Macheret S.O., Miles R.B., "Optimization of Dielectric Barrier Discharge Plasma Actuators Driven by Repetitive Nanosecond Pulses," AIAA-2007-633, Reno NV, January 2007.

[9] Soloviev V.R., Krivtsov V.M, Konchakov A.M., Malmuth N.D., "Surface Barrier Discharge Simulation in Air for Constant Applied Voltage," AIAA-2008-1378, Reno NV, January 2008.

[10] Soloviev V.R., Konchakov A.M., Krivtsov V.M, Aleksandrov N.L., "Numerical Simulation of a Surface Barrier Discharge in Air," *Plasma Physics Reports*, V.34, 2008, No.7, pp.594-608.

[11] Aleksandrov N.L., Visikailo F.I., Islamov R.Sh., Kochetov I.V., Napartovich A.P., Pevgov V.G., "Electron Distribution Function in Mixture N_2:O_2=4:1," *High Temp.*, Vol. 19, №1, 1981, pp. 22-27.

[12] Aleksandrov N.L., Bazelian A.E., Bazelian E.M., Kochetov I.V., "Long Streamer Modeling in Atmospheric Pressure Gas," *Plasma Physics Rep.*, Vol. 21, 1995, pp. 60 -80.

[13] Kossyi I.A., Kostinsky A.Yu., Matveyev A.A., Silakov V.P., "Kinetic Scheme of the Non-Equilibrium Discharge in Nitrogen-Oxygen Mixtures", *Plasma Sources Sci. Technol.*, Vol. 1, 1992, P. 207

[14] Georghiou G.E., Papadakis A.P., Morrow R., Metaxas A.C., "Numerical Modeling of Atmospheric Pressure Gas Discharges Leading to Plasma Production", *J. Phys. D: Appl. Phys.*, Vol. 38, 2005, R303-R328.

[15] Zhelezniak M.B., Mnatsakanian A.Kh., Sizykh S.V., "Photoionization of Nitrogen-Oxygen Mixture by Gas Discharge Radiation," *High Temp.*, Vol. 20, No.3, 1982, p. 423.

[16] Birdsall Ch.K, Langdon A.B., *Plasma Physics*, *Via Computer Simulation.* McGrow-Hill Book Company, 1985.

[17] Philippov A.V., Dyatko N.A., Pal A.Ph., Starostin A.N., "Self-consistent Model of a Dust Particles Charging at Enhanced Pressures on the Basis of Moment Technique," *Plasma Physics Rep.*, Vol. 29, 2003, pp.214 -226.

[18] Gibalov V.I., Pietsch G.J., "The Development of Dielectric Barrier Discharges in Gas Gaps and on Surfaces," *J. Phys. D: Appl. Phys.*, Vol. 33, 2000, pp.2618-2636.

[19] Roe, P.L., "Characteristic Based Schemes for the Euler Equations," Annual Review of Fluid Mech., Vol. 18, 1986, pp. 337-365.

[20] Chakravarthy, S.R., and Osher, S., "A New Class of High Accuracy TVD Schemes for Hyperbolic Conservation Laws," AIAA Paper No. 85-0363, 1985.

[21] Weiss, J.M., Maruszewski, J.P., and Smith, W.A., "Implicit Solution of the Navier-Stokes Equations on Unstructured Meshes," AIAA Paper No. 97-2103, 1997.

[22] Visbal, M.R., and Gaitonde, D.V., "Control of Vortical Flows Using Simulated Plasma Actuators," AIAA- 2006-505, Jan. 2006 Reno, NV.

[23] Budovsky A.D., Zanin B.Yu., Zverkov I.D., Kozlov V.V., Maslov A.A., and Postnikov B.V., Sidorenko A.A., "Plasma Control of Vortex Flow on Delta-Wing at High Angles of Attack," International Conference on Methods of Aerophysical Research (ICMAR). Novosibirsk, Russia. 2008.

Personnel Supported

V.R. Soloviev and V.M. Krivtsov – SDBD modeling

A.V. Fedorov and V.G. Soudakov – flow control modeling

Transitions

Examples of Use in Technology Applications

- Our transition prediction techniques are being applied to hypersonic vehicles by Don Picetti and others of Boeing and are now being part of Boeing's automated design program (BVIDs)
- Our plasma modeling and experiments have played an important part of Boeing programs.

Discoveries, Inventions, and Patent Disclosures

- "Surface Plasma Discharge for Controlling Leading Edge Contamination and Crossflow Instabilities for Laminar Flow, US 6,805,325, B1, issued October 19, 2004
- "Surface Discharge for Controlling Vortex Asymmetry," US 6,796,532 B2, issued September 28, 2004

Publications

P1. Shalaev, V., Fedorov, A., Malmuth, N., and Shalaev, I., "Mechanism of Forebody Nose Vortex Symmetry Breaking Relevant Plasma Flow Control," AIAA Paper No. 2004-0842, Reno NV, Jan. 2004.

P2. Maslov, A.A., Zanin, B.Yu., Sidorenko, A.A., Fomichev, V.P., Postnikov, B.V., and Malmuth, N., "Plasma Control of Separated Flow Asymmetry on a Cone at High Angle of Attack," AIAA Paper No. 2004-0843, Reno NV, Jan. 2004.

P3. Malmuth, N., Krivtsov, V., and Soloviev, V., "Quick, Gridless Estimations of MHD Effects on Hypersonic Inlet Ramp Shocks," AIAA Paper No. 2004-0862, Reno NV, Jan. 2004.

P4. Zhakharov, S.B., Fedorov, A.V., and Malmuth, N.D., "Modeling of Forebody Nose Symmetry Breaking Using Conical Navier-Stokes Solutions," AIAA Paper No. 2006-1257, Reno NV, Jan. 2006.

P5. Malmuth, N., "Theoretical Aerodynamics in Today's Real World, Opportunities and Challenges," Julian D. Cole Lecture, *AIAA J.*, **44**, No.7, 2006, pp. 1377-1392

P6. Malmuth, N.D., Zhakharov, S.B., and Fedorov, A.V., "Conical Navier-Stokes Modeling of Forebody Vortex Symmetry Plasma Control," AIAA Paper No. 2007-0219, Reno NV, Jan. 2007.

P7. Soloviev, V.R., Krivtsov, V.M, Konchakov, A.M., and Malmuth, N.D., "Surface Barrier Discharge Simulation in Air for Constant Applied Voltage", AIAA Paper No. 2008- 1378, Reno NV, Jan. 2008.

P8. Soloviev V.R., Konchakov A.M., Krivtsov V.M, Aleksandrov N.L., "Numerical Simulation of a Surface Barrier Discharge in Air", *Plasma Physics Reports*, V.34, 2008, No.7, pp.594-608.

P9. Soloviev, V.R., Krivtsov, “Features of a Surface Barrier Discharge Modeling”, AIAA Paper No. 2009-0842, Orlando Fl, Jan. 2009.
P10. Fedorov, A.V., and Soudakov, V.G., “Modeling of Plasma Flow Control over a High-Speed Delta Wing,” AIAA Paper No. 2009-0699, Orlando Fl, Jan. 2009.